SANDIA REPORT
SAND2015-7567
Unlimited Release
Printed September 2015

New Radiological Material Detection Technologies for Nuclear Forensics: Remote Optical Imaging and Graphene-Based Sensors

Richard K. Harrison, Jeffrey B. Martin, Dora Wiemann, Junoh Choi and Steve Howell

Projects: SNL.14.006, SNL.14.007, WBS 3.2.1, WBS 3.2.2

Prepared by
Sandia National Laboratories
Albuquerque, New Mexico 87185 and Livermore, California 94550

Sandia National Laboratories is a multi-program laboratory managed and operated by Sandia Corporation, a wholly owned subsidiary of Lockheed Martin Corporation, for the U.S. Department of Energy's National Nuclear Security Administration under contract DE-AC04-94AL85000.

Issued by Sandia National Laboratories, operated for the United States Department of Energy by Sandia Corporation.

Available to DOE and DOE contractors from
U.S. Department of Energy
Office of Scientific and Technical Information
P.O. Box 62
Oak Ridge, TN 37831

Telephone: (865) 576-8401
Facsimile: (865) 576-5728
E-Mail: reports@osti.gov
Online ordering: http://www.osti.gov/scitech

Available to the public from
U.S. Department of Commerce
National Technical Information Service
5301 Shawnee Rd
Alexandria, VA 22312

Telephone: (800) 553-6847
Facsimile: (703) 605-6900
E-Mail: orders@ntis.gov
Online order: http://www.ntis.gov/search

SAND2015-7567
Unlimited Release
Printed September 2015

New Radiological Material Detection Technologies for Nuclear Forensics: Remote Optical Imaging and Graphene-Based Sensors

Richard K. Harrison, Jeffrey B. Martin, Dora Wiemann,
Nuclear Forensics R&D

Junoh Choi
Optics and Sensor Engineering

Steve Howell
Radiation Hard CMOS Technology

Sandia National Laboratories
P.O. Box 5800
Albuquerque, New Mexico 87185-MS0968

Abstract

We developed new detector technologies to identify the presence of radioactive materials for nuclear forensics applications. First, we investigated an optical radiation detection technique based on imaging nitrogen fluorescence excited by ionizing radiation. We demonstrated optical detection in air under indoor and outdoor conditions for alpha particles and gamma radiation at distances up to 75 meters. We also contributed to the development of next generation systems and concepts that could enable remote detection at distances greater than 1 km, and originated a concept that could enable daytime operation of the technique. A second area of research was the development of room-temperature graphene-based sensors for radiation detection and measurement. In this project, we observed tunable optical and charged particle detection, and developed improved devices. With further development, the advancements described in this report could enable new capabilities for nuclear forensics applications.

ACKNOWLEDGMENTS

We would like to thank our mentor, Jeff Martin, for his advice and leadership throughout this project, as well as Karen Rogers, our manager, for her guidance and support. We also acknowledge the contributions of our team members in completing this work. Specifically, Dora Wiemann was instrumental in carrying out many of the experiments described in this report. Junoh Choi designed the pathfinder optical telescope and was also a major contributor to experimental efforts. The Summer 2014 MSTIC student helped run the indoor optical radiation detection experiments at GIF, and contributed to the modeling effort, and 2014 DHS Undergraduate Fellow performed a number of experiments showing the capabilities of the optical spectroscopy project. Safety Coordinator Taffey Maddox helped us perform our work safely. Don Hanson and Maryla Wasiolek of the Gamma Irradiation Facility were great partners to work with and the GIF experiments could not have happened without their enthusiastic contributions. Steve Howell leads the GFET research effort, and Ken Armijo was our collaborator in the optical emission spectroscopy projects and solar spectral measurement projects. We also acknowledge the work of the optomechanics group, especially Andrew McCants and Ted Winrow, who constructed the ROSIR telescope. Finally, we acknowledge the support of the DHS DNDO National Technical Nuclear Forensics Center through the Expertise Development Program. As the sponsor of this research, they graciously provided us with the freedom and resources to pursue this research and develop these capabilities.

CONTENTS

FIGURES

TABLES

NOMENCLATURE

AOD	Aerosol optical depth
CCD	Charge-coupled device
COTS	Commercial off-the-shelf (i.e., can be readily purchased in the open market)
CPS	Counts per second
CZT	Cadmium zinc telluride
GFET	Graphene field-effect transistor
GIF	Gamma Irradiation Facility
IAEA	International Atomic Energy Agency
LED	Light emitting diode
LIDAR	Laser Imaging, Detection and Ranging
MCNP	Monte Carlo N-Particle
ODR	Optical detection of radiation
PNNL	Pacific Northwest National Laboratories
RDD	Radiation dispersal device
SNL	Sandia National Laboratories
SNR	Signal to Noise Ratio
TLD	Thermoluminescent dosimeter
UV	Ultraviolet

1. INTRODUCTION

During this three-year project, we investigated alternative signatures and new technologies for the detection of radiation and radiological materials for post-detonation nuclear forensics applications. Disruptive improvements in radiation detection could significantly impact key nuclear forensics timelines by accelerating debris and plume collections and through evaluating nuclear materials in the field.

Developing new technologies for nuclear forensics represents a unique challenge because of three primary reasons: 1) new technologies cannot be tested in real-life conditions on test nuclear detonations, 2) technologies developed during the period of nuclear weapons testing will always be trusted more than anything developed later, and 3) in the terrible event of a nuclear or radiological attack, the timelines for existing technologies are too slow and the answer too important to not pursue new technologies. With these conflicting imperatives, we approach nuclear forensics research and development with the ideas of complementarity, where new technologies are designed to augment existing capabilities to benefit the overall mission, and the ability to validate, which is more crucial for the nuclear forensics application than others because of the importance of the answer and the dearth of relevant testing options. We embraced this philosophy in our work over the course of this fellowship in the development of alternative technologies for radiation and radiological material detection.

Our research in nuclear forensics is directed along three main technical thrusts. The primary body of work covered in this report focuses on the detection of ionizing radiation through optical imaging of air fluorescence, which we investigated because of its potential to extend the range at which radiation can be detected by an order of magnitude. We also present our efforts to develop graphene field effect transistor radiation sensors for high resolution room temperature gamma spectroscopy. Lastly, we discuss research into the use of optical emission spectroscopy for elemental analysis and plasma diagnostics, which we pursued through mentoring undergraduate student interns. The common thread of these research projects is the application of new technologies to address specific challenges in nuclear forensics. This report describes our progress in each of these research areas through new experimental results, concepts developed, and improvements in capabilities.

2. OPTICAL DETECTION OF IONIZING RADIATION

2.1 Phenomenology

In the course of this project, we investigated an optical technique for the detection of ionizing radiation for post-detonation nuclear forensics applications. The optical detection of radiation (ODR) is based on the ultraviolet fluorescence of nitrogen in the atmosphere induced by ionizing radiation interacting with the air. Ultraviolet (UV) photons emitted in this process can be detected using optical instruments to identify the presence and intensity of the radiation field. The benefit of air fluorescence (a secondary signal) to remotely detect radiation stems from the several kilometer range of UV light in sea-level air, which is orders of magnitude longer than the attenuation lengths of ionizing radiation (the primary emission).

The premise behind ODR is that ionizing radiation deposits energy in the ambient air that can excite nitrogen molecules to forbidden energy states that decay radiatively. The strongest emissions in this process occur in the 337 nm, 357 nm, 316 nm, and 391 nm bands in the ultraviolet. Figure 1 shows the principle peaks and relative yields of the nitrogen fluorescence spectrum.

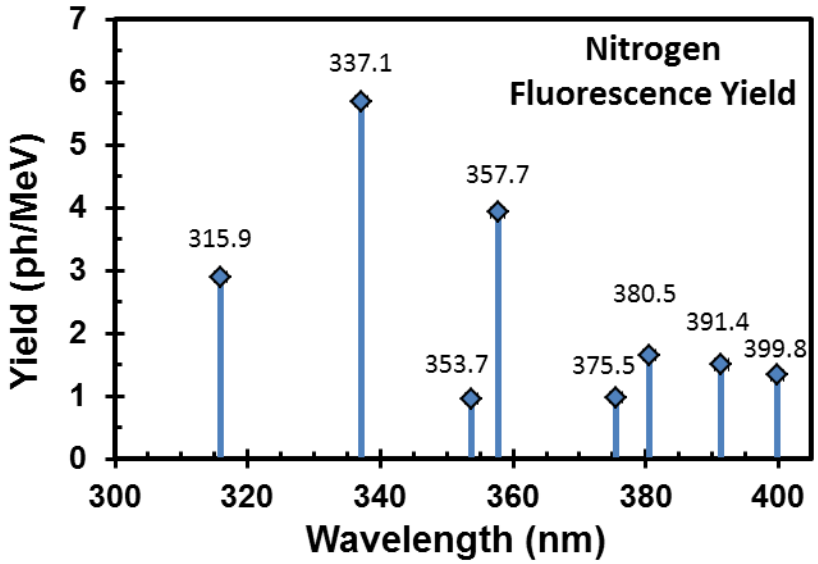

Figure 1: Nitrogen fluorescence yield for the principle emission peaks in the UV.
The values were calculated for the conditions in Albuquerque, NM.[1]

In the ODR technique, the air serves a scintillator, where 17 UV photons are emitted per MeV of ionizing radiation deposited in the air at sea level. The scintillation emission and density of air are low relative to common scintillating detector materials like thallium-doped sodium iodide (NaI(Tl)), which has a scintillation yield of approximately 20,000 photons per MeV of deposited energy. However, the immense volume of dosed air relative to typical detector sizes mitigates this low efficiency issue.

The challenges of detecting ionizing radiation remotely are significant, primarily because the limited range of ionizing radiation in the atmosphere. The exponential attenuation lengths for gamma rays and neutrons are 150 meters and 50 meters, respectively, while the range of beta

particles is 3 meters and only 5 centimeters for alpha particles. Within these distances, the primary radiation signals can and should be used directly to characterize the activity and radioisotope of a given source, but there is a transition point where the intensity of the primary radiation signature is reduced to undetectable levels and the presence of ionizing radiation can be much more readily detected using the induced secondary optical emissions. The ODR technique offers a path to detect radiation well beyond the limit for conventional detectors.

2.2 History

The scientific history of the radiation-induced air fluorescence phenomenon dates back to the Manhattan project. Air fluorescence following a nuclear detonation is known as 'Teller light' because Edward Teller predicted and observed this phenomenon at the Trinity test[2]. Subsequently, the possibility that cosmic rays could also induce air fluorescence was investigated in the lab of Kenneth Greisen, who witnessed the Trinity test[2,3]. The technique has since been investigated in depth in the ultra-high energy cosmic ray detection community, where nitrogen fluorescence 'showers' caused by cascades of energetic particles can be used to track ultra–high–energy cosmic rays interacting with the Earth's atmosphere. Interestingly, the first experimental observation of cosmic ray induced optical fluorescence occurred just outside of Albuquerque, only 20 miles from Sandia National Laboratories[4]. Increasingly capable scientific facilities have been built to measure this phenomenon, starting with the Fly's Eye facility developed at the University of Utah[5], the Pierre Auger observatory in Argentina[6], and the JEM-EUSO sensor that will soon be fielded on the International Space Station[7]. The astronomical community has provided a great deal of phenomenological data on yield, backgrounds, and spectral emission ratios for ionizing radiation-induced nitrogen fluorescence[8,9].

The ODR technique was also considered for terrestrial use in detecting radiological materials. A 2003 Pacific Northwest National Laboratories (PNNL) report on alternative radiation detection methods explored the possibility of radiation detection using optical techniques and suggested that it could be feasible detection method[10]. Since that time, research has focused on the indoor detection of charged particle radiation for contamination detection[11,12,13] and for special nuclear material tracking[14]. Another recent use of the ODR technique is for visualizing therapeutic radiation beams directly using the air scintillation of X-ray beams and electrons in ambient air[15]. These indoor cases take advantage of low backgrounds and relatively high linear energy transfer, which corresponds to high local dose rates, to attain a sufficient signal to noise ratio (SNR). However, while these demonstrations are useful for comparisons, applying an ODR approach to the problem of remote outdoor detection of radioactive materials using a mobile sensor represents a significant challenge because of the dramatically higher UV backgrounds, diffuse sources, slowly varying signal and kilometer–scale distances.

In the past decade, dramatic technological improvements have improved the outlook for the ODR technique. First, the advances in CCD camera technologies have been enormous, including the development of back-illumination, thinned detector geometries that have enabled greater than 60 percent quantum efficiencies in the UV. Additionally, huge strides in Peltier (thermoelectric) cooling now permit robust, off-the-shelf cooling to -100 °C, a level that was only feasible with liquid nitrogen ten years ago. This level of cooling significantly reduces the dark noise and enables long exposure imaging. Finally, high transmission (greater than 90 percent), narrow-band UV filters have become commercially available. Combined, these factors improve the

prospects of the ODR technique by increasing the number and proportion of measurable photons to achieve higher SNR than were historically possible.

2.3 Advantages of the ODR Technique

The significant differences between the transport and collection of optical photons when compared to ionizing radiation have profound implications for the capabilities and limitations of the ODR technique. Optical radiation detection has several features that differentiate this indirect technique from conventional radiation detection methods. First and foremost, optical radiation detection is interesting primarily for remote detection applications. The principle differentiator of the ODR method is the ability to detect dose outside of the radiation-dosed region, in stark contrast to direct ionizing radiation detection. This capability implies that the dose to personnel could be reduced while identifying high-dose regions from a distance; it also implies that the technique could potentially be used to detect radiation sources around shielding, where a high dose region adjacent to the source could be detected (i.e., an optical path to the dosed region is required, but not necessarily to the source itself).

There are several additional advantages of the ODR technique for remotely detecting ionizing radiation beyond just the increase in detectable range. This technique enables the use of relatively inexpensive, technologically mature commercial-off-the-shelf (COTS) optics to collect the air fluorescence signature and image the dose in air. Relatively light weight systems can be used to achieve a large collection aperture, as UV photons (300 to 400 nm) can be collected, refracted, reflected, focused and imaged like optical wavelength photons (400 to 700 nm) due to their similar optical properties. Additionally, a multispectral ODR imaging system could be used to overlay the radiation dose map over a visible image of a scene to provide situational awareness of the radiation dose in an area. Unlike ionizing radiation, the optical photons emitted from a dosed region can be focused such that the optical signal 'observed' by a given pixel in the CCD sensor increases with range to mitigate the geometrical $1/R^2$ loss in signal intensity, which is an intriguing feature of these systems. Additionally, optical techniques are inherently direction sensitive. While gamma ray or neutron imaging systems provide only coarse direction of a source, the ODR technique offers better than 0.001 degree resolution. These advantages could address nuclear forensics goals by substantially improving the speed of searching for radiological dispersal devices, detecting post-detonation plumes or mapping fallout.

2.4 Challenges of the ODR Technique

The primary challenges facing this work are the low 0.006% efficiency of nitrogen fluorescence emission and the relatively high man-made and natural backgrounds against which the fluorescence signal must be discriminated. The optical background is much higher in terms of detectable counts per second than the natural radiation background. The high background and relatively weak signal implies that many applications of optical radiation detection will be background limited (as opposed to signal limited), and that this technique will primarily be limited to night-time, low man-made light conditions. Additionally, distributed low activity sources may be difficult to distinguish from slight variations in ambient light levels. To address these challenges, we studied the UV background and identified several techniques for improving signal-to-noise ratios. Background reduction strategies can be employed to mitigate the effect of high backgrounds on radiation detection and imaging, and narrow band filters of <10 nm can be chosen to eliminate out-of-band light that does not contain a nitrogen emission line of interest.

These filters can be used in conjunction in a multi-spectral imaging approach to identify regions where the detected light follows the expected fluorescence line ratios between the different UV emission bands for radiofluorescence, which can provide improved confidence in identifying ionizing radiation sources.

Other limitations of this technique revolve around the differences between optical and conventional 'direct' radiation detection. For example, UV photons generated by ionizing radiation give a response proportional to the dose in the air but do not differentiate between the types of ionizing radiation. With ODR, some distinction could be made based on the spatial extent of the detected signal such that the type (*e.g.* alpha, beta, gamma or neutron) of radiation emission for an unknown source may be inferred using spatial filtering. Additionally, the challenges of interpreting a spatially-varying three-dimensional radiation dose field using a two-dimensional imaging sensor complicate the analysis of ODR signals. The images acquired in ODR represent volumetric integrals of the radiation dose rate for a 'voxel' that corresponds to a pixel on the camera, where the length of the voxel is given by the depth of field of the optical system. This effect is another subtle but important difference in the application of the ODR technique, with implications including the effects of shadowing and the potential to use short depth-of-field optics or scanning depth sectioning 'confocal' approaches to construct a three-dimensional data cube representing the spatially varying radiation dose. Finally, the use of optical elements in the detector will be more sensitive to vibration and dust and require additional effort to make robust and field than typical radiation sensors.

2.5 Indoor ODR of Charged Particles – Analysis of Results

At the outset of the project, we needed a facility to perform ODR development and testing. As our first milestone, we acquired and equipped a dedicated nuclear forensics laboratory with capabilities for performing both radiation and optical work. The 1,000+ square foot research and development lab space has various radioactive sources, a floating optical table for precision alignment, lasers up to Class IV, radiation spectrometers, optical characterization equipment, and chemical and sample preparation areas. The lab enabled ODR research by providing the space and facilities necessary for development and testing.

We first demonstrated the ODR technique by imaging the radiation dose in air surrounding a polonium-210 (^{210}Po) alpha emitter in a dark indoor lab environment. This source was selected because of the strong, confined radiation fields present around the source due to the short range of alphas in air. These experiments were designed to gain practical experience in the detection of radiation through UV optical detection and imaging. The ^{210}Po source (NRD Static Control, Model 1U400), which is typically sold as a static eliminator, had an initial activity of 500 microcuries (μCi). The radiation dose rates for a small volume very near the source surface is comparable to what may be found around a radiation dispersal device (RDD). After a review of the related literature[11,12], we set up a darkroom facility to enable low-light level testing, and developed an optical system for UV detection consisting of a Princeton Instruments ProEM (512B_ExCelon) camera with high UV quantum efficiency, a Schneider Kreuznach camera lens (70 mm focal length), and a Chroma UV pass filter (325 – 375 nm, 2-inch diameter). After the optical background was well characterized, we captured images of the nitrogen fluorescence emanating from the radiation dose field, directly showing the range and energy deposition of alphas in air (Figure 2a). Interestingly, our high resolution image can capture the effect of the metal guard bars over the source on the detected signal (Figure 2b).

These images provided a great deal of information on the detection process, image analysis, and the operation of the charge-coupled device (CCD) camera. In the laboratory's dark conditions, the radiation could be detected in as little as 10 seconds, but longer exposure images provided a much better indication of the dose profile. The source was imaged at a distance of 1.2 meters, which is 40× the range in air of the alpha particles, demonstrating the detection of radiation outside of the irradiated region.

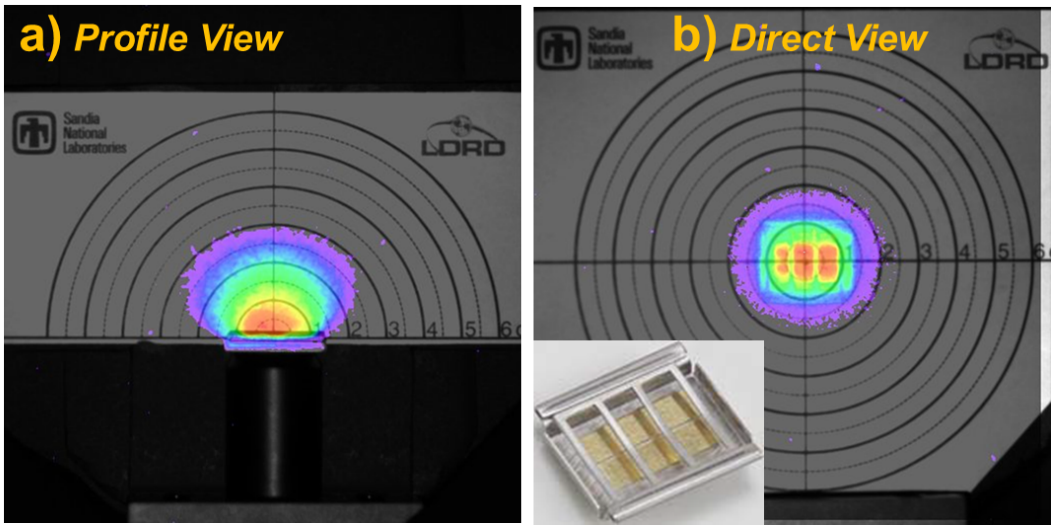

Figure 2: False color images of the radiation dose profile from a ^{210}Po alpha emitter.
a) and b) show the net background-subtracted, low-pass filtered signals resulting from a one hour exposure overlaid on a target to show the spatial extent of the radiation field. The numbers on the targets indicate radius in cm, and the inset in b) shows the alpha source itself, where the ^{210}Po is encapsulated in the gold layer and the aluminum guard bars are also visible.

To understand the ODR process, we developed a 3D Matlab model of the ^{210}Po static ionizer alpha emission and radiation deposition in the air using a randomized Monte Carlo-like statistical approach to model the alpha absorption process. In this model, we use the National Institute for Standards and Technology ASTAR library[16] for alpha interactions both within the encapsulation layers (shown in Figure 3a) and the surrounding air as a function of energy to find the local energy deposition at each point in space around the source. While this program is a first step in estimating the local energy deposition, we found that the modeled dose profile qualitatively agreed with measurements. (Figure 3b and Figure 3c).

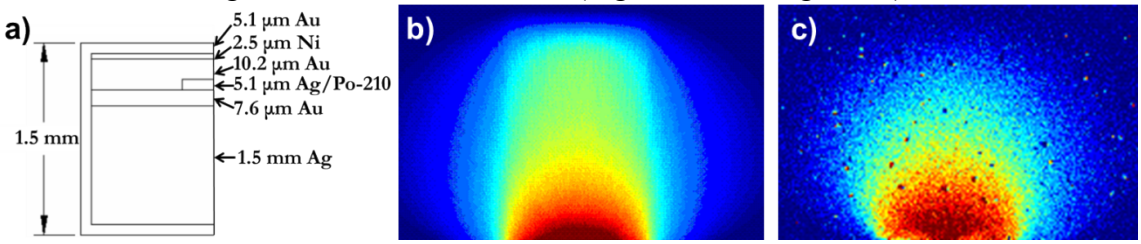

Figure 3: Computational results for estimating expected signals.
a) Schematic showing the structure of the ^{210}Po static ionizer source. b) Simulated optical emission from excited nitrogen around an alpha emitter at a distance of 1.2 meters using 2 million alpha particles. c) Observed UV fluorescence image for the same conditions.

Subsequently, we performed a set of experiments to practically evaluate the usage of the ODR technique. Figure 4 presents the improvement in the image quality that is observed with exposure time, along with the calculated signal to noise ratio (SNR) for the images. Here, we calculate the SNR as the quotient of the averaged pixel value in the source region of interest to the background noise level in a region far from the source. The background noise is determined as the root mean square value between two 'source-free' control images.

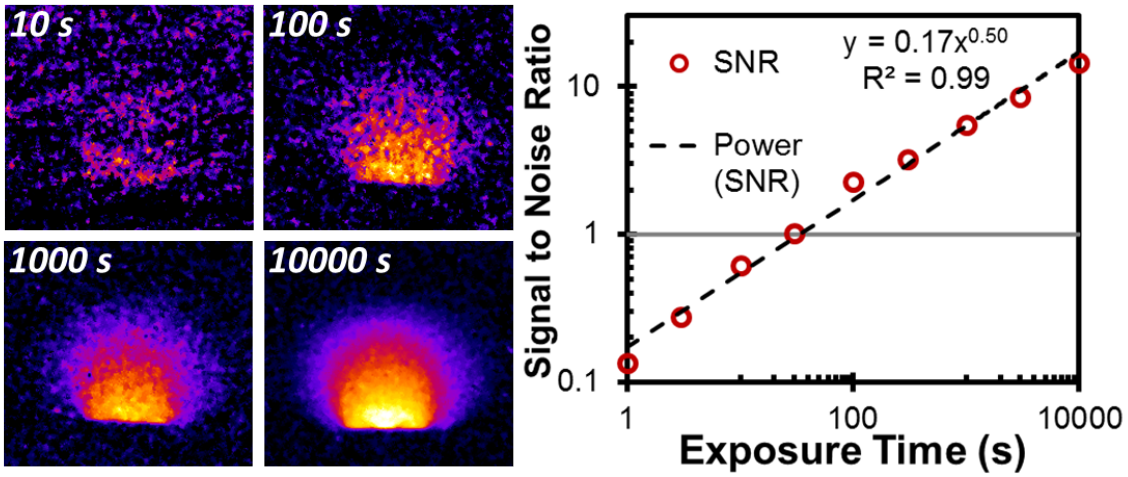

Figure 4: Time dependence of the detected optical signal.
False color images of the radiation dose profile from a ^{210}Po source and the corresponding SNR values as a function of time. The net background subtracted signals were low-pass filtered.

The results presented in Figure 4 reveal several important features. First, as the exposure time increases, the emission volume fills in, showing the statistical nature of radiation absorption and fluorescence emission. Second, the log-log linearity of the SNR to exposure time plot and square root dependence, and the power law fit provides the expected value for a linear signal and random noise. The SNR power law fit with an exponent of 0.5 occurs because the signal increases linearly with time, but the noise will only increase as the square root of the exposure time. This trend suggests that our optical detector is operating in the shot noise limited regime, and that the detection is optimized for these given optical conditions.

The initial analysis of radiation-induced nitrogen fluorescence images also included an evaluation of the SNR obtainable as a function of the number of combined pixels in an image, known as the binning. The ProEM camera allows for on-chip binning of the observed signal, which can result in rapid detection and higher SNR values because of a reduction in the effective noise. The benefit peaks as the bin size approaches the size of the radiation dosed area. Figure 5 shows the increase in SNR obtainable with increasing bin size. A similar effect can be observed with purely numerical binning, but the performance is improved if the binning is performed on chip to reduce read-out noise.

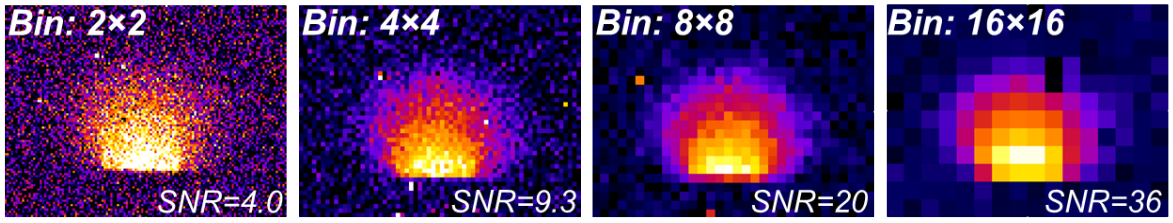

Figure 5: Effect of bin size on the image resolution and signal to noise ratio.
The false color images show the radiation dose profile from a ^{210}Po alpha emitter and the corresponding SNR values as a function of bin size for a 300 second exposure time.

One of our early claims regarding the possibilities of optical radiation detection was that the imaged range of radiation in air might be correlated with the energy of the radiation particle. Our alpha source offers a prime opportunity to test this hypothesis because the alpha energy can be easily attenuated with thin shielding layers. To examine this possibility, we performed a set of radiation-induced fluorescence measurements with shielding over the alpha emitter. We used up to two layers of an 8 µm thick aluminum foil (Alfa Aesar, 99.0%) to adjust the energy of the penetrating alphas. Figure 6 shows a comparison of the images and range of alphas in air as a function of shielding thickness, demonstrating the range attenuation that occurs for emitted radiation with different energies. We calculate an average alpha particle energy of 4.5 MeV for alphas after escaping the encapsulating films, 3 MeV after exiting one layer of aluminum and 0.8 MeV after exiting two layers of aluminum. The calculated ranges of 4.5, 3 and 0.8 MeV alpha particles in air are 3, 1.6 and 0.5 cm, respectively. The experimentally detected ranges coincide with the expected values. This agreement indicates that radiation-induced fluorescence could be used to directly image the range of charged particles in air and potentially distinguish the energy and type of radiation interacting with the atmosphere.

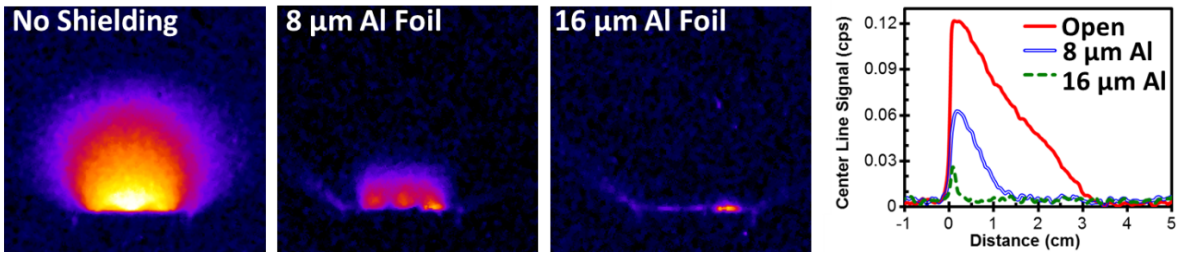

Figure 6: Effect of shielding on the ODR detected range of alphas in air.
The false color images depict the radiation dose profile from a ^{210}Po alpha emitter for different amounts of shielding for a 10000 s exposure. The chart shows the centerline signal in the vertical direction for the three images. The range of alphas in air can be clearly identified from the distance at which the signal approaches the background.

It should be noted that there is a 6 mm tall aluminum guard around the perimeter of the source (Figure 2b inset) which blocks light emitted from the air between the source and the guard bars. This air gap, along with the encapsulation layers, serves to absorb some of the energy from the alphas that are initially born at 5.3 MeV. Although the applications of measuring low energy alpha particles may be limited to indoor contamination detection, the demonstration of the capability to visually detect alpha–induced fluorescence in air shows that a similar technique might be used to discriminate neutrons from gamma rays, or to have some capability to tell

between low and high energy gamma rays in long-range applications. Furthermore, there may be applications where detecting short range fission products in air from a distance could be useful.

We subsequently investigated the scaling of the optical emission with the source activity using two different ^{210}Po sources with different activities. By imaging both sources simultaneously, we found a significant difference in the optical count rate for the two different strength sources, reflecting that the optical count rate is proportional to the source activity. However, the spatial extent of the UV fluorescence emission, corresponding to the range in air, does not change with source activity, as expected. These results are presented in Figure 7.

The capability for dose rate discrimination, at least in these controlled conditions, is an initial step towards the goal of correlating the radiation energy deposition rate with the photon detection. A complete understanding of this relationship will require further development of a detector model, lens depth of field, atmospheric transmission, and quantitative photon emission values for different radiation types. We started work on calculating atmospheric absorption and the transport of radiation and UV photons, but developing a full model of the radiation energy deposition, excitation of nitrogen molecule energy levels, and photon emission is a process that will require additional investigation.

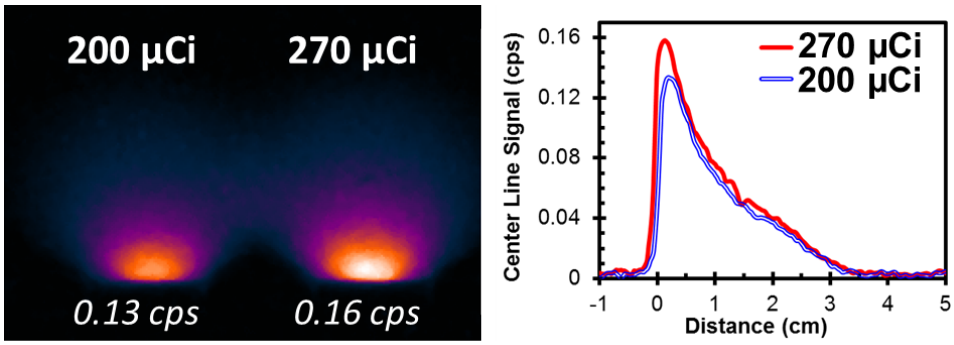

Figure 7: Results from imaging two alpha emitters with different activities simultaneously.

The false color images show the radiation dose profiles from two ^{210}Po alpha emitters of different activities. The chart shows the centerline signal in the vertical direction for the sources.

2.6 Indoor ODR of Charged Particles – Component Identification

An imaging system for optical radiation detection needs to have high transmission efficiency in the ultraviolet. Unfortunately, modern commercial camera lens systems are typically assembled together using optical cements designed to block UV light. Ultraviolet light is usually considered a source of noise or 'haze' for most photographic applications, but there is a small sub-community of amateur photographers who focus ultraviolet photography. This sub-community typically photographs flowers, which often reveal startlingly different patterns in the UV, a band visible to birds and insects[17,18].

If UV transmission can be achieved, camera lenses are an excellent option for developing a compact ODR system, as the focus position and aperture can typically be adjusted to cover a range of scenarios. We thus tested a range of COTS lenses for their UV transmission. Most of the lenses we tested could be used to detect the low intensity nitrogen emission lines around 400

nm, but passed very little UV light. However, we found that older lenses (without the UV absorbing cement), lenses with simple optical designs, and reflective element or other specially built lenses can have excellent UV transmission and imaging capabilities. We experimented with the collimated output from a 380 nm fiber coupled LED source and a UV pass-band filter to identify promising lens candidates. The focus was kept at infinity for the collimated source, where the beam was smaller than the lens aperture, and the testing distance was 1.5 m. We found that the transmission varied by more than an order of magnitude for the tested lenses (Figure 8).

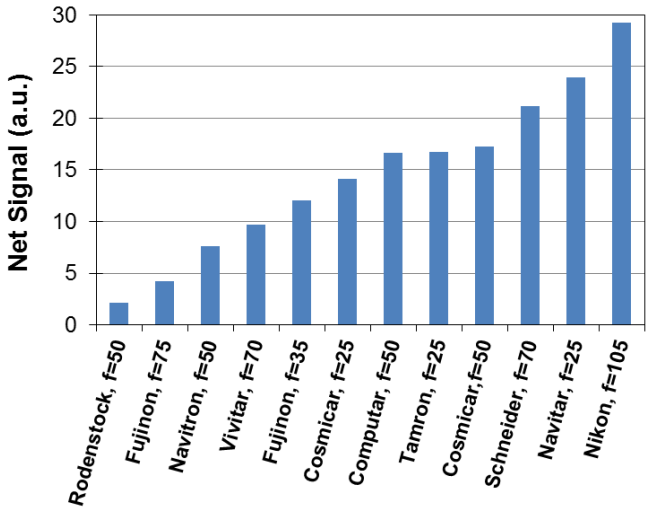

Figure 8: UV transmission testing of COTS camera lenses.
The figure shows the relative signal from a collimated LED at 380 nm for a subset of 12 of the tested commercial camera lenses, with lens focal lengths given in mm.

Several lenses, including the specially designed 105 mm focal length Nikon UV Nikkor and the 25 mm focal length Navitar, were found to have high ultraviolet throughput and high-resolution imaging capabilities. The Nikon UV Nikkor 105 was found to have a transmission efficiency of 81% using the 380 nm LED, and the lens specifications indicate that the transmission efficiency is flat across the 300 – 400 nm spectral range.

The experiments testing the UV optical transmission and imaging capability of commercial camera lenses led naturally to further lab testing of these systems for imaging the nitrogen fluorescence emitted from ionizing radiation interacting with the air. We measured the optical emission from a ^{210}Po alpha source, now decayed to 80 μCi, in 15 minute exposures using each of the previously tested lenses. The field of view is inversely related to the focal length, and the smaller f-stops, corresponding to larger effective apertures, yielded higher signal levels as expected. Figure 9 shows a series of images from three lenses at a distance of 1.2 meters from the source. The variation in the field of view of these lenses, all of which could be used to obtain high resolution images of the fluorescence emission, may be useful for different range scenarios or radiation particle types. These experiments demonstrated that radiation field imaging can be accomplished with a compact system leveraging commercial camera lenses, provided the lens was tested for UV resolving power and transmission efficiency.

The indoor tests of the ODR technique are useful for identifying some of the capabilities and limits of optical radiation detection. Specifically, we found that analyzing and processing

optical images of fluorescence emitted from radiation energy deposited in air taken in a lab setting is an important part of the detection process, identified components for building an ODR system, and demonstrated that fluorescence emission is proportional to radiation dose.

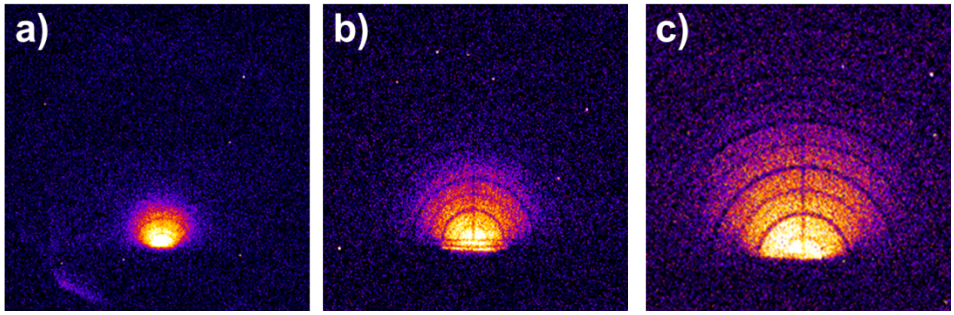

Figure 9: Profile-view ODR images of an alpha emitter in front of a target.
The three commercial lenses used in this case are a) Navitar, f=25 mm, f/0.95, b) Computar, f=50 mm, f/1.3, and c) Telephoto, f=75 mm, f/1.2.

2.7 Outdoor ODR of Charged Particles – Optical Transport Calculations

One of the issues that can affect the detected signal for the ODR technique is the atmospheric transmission, which can vary depending on conditions such as humidity, altitude, and air quality. Aerosols have the most significant effect on transmissivity. The density, material and size distribution all affect the optical properties of particulates in the air, and these parameters are themselves function of temperature, location, season and wind-speed. At ranges of less than 500 m, the attenuation of UV light is negligible under typical atmospheric conditions, but at longer distances, then scattering losses can be significant. We thus investigated methods of measuring, evaluating and calculating the atmospheric transport of UV photons.

In this project, we used MODTRAN, one of the preeminent optical transport modeling software packages, to simulate the spectrally resolved solar irradiance under realistic conditions for Albuquerque, New Mexico. We then benchmarked our calculated results to measured solar spectra through a collaboration with Sandia's solar characterization group (6112) to excellent agreement (Figure 10a)[19]. These validated simulations provided a strong indication that we can model the atmospheric constituents accurately, and that MODTRAN simulations could then also be used to calculate the photon transport as a function of distance and wavelength (Figure 10b), at least under the dry, high altitude conditions we studied. Further investigation of this technique should include humid sea-level or high pollution conditions to validate the method for other locations.

We also studied the effects of atmospheric components that can vary for different geographical locations and times of the year. Specifically, we simulated the effects of varying the particulate, water vapor and ozone concentrations. Though dust is the only one of these components that strongly affects the UV region of our primary interest, understanding each of these atmospheric constituents helps us create a higher fidelity atmospheric model. Water vapor primarily affects long wavelength, near-infrared optical transmission, with major absorption bands at 720, 820, 940, 1130 and 1370 nm (which can be seen as dips in Figure 10a). The atmospheric water vapor content can strongly from one location to another, ranging an order of magnitude between desert and equatorial humid conditions. Ozone absorbs primarily in the 500 –

700 nm band, and also for wavelengths shorter than 325 nm. Recent work suggests that ozone concentrations can be elevated near urban centers[20], indicating that it could be a relevant factor. In Albuquerque's desert-like conditions, the visibility can be strongly affected by the wind speed, which picks up and drives sand dust and particles through the air. In this model, higher wind speeds pick up more particles, but the average particle size also increases. In contrast to the discrete bands observed for water vapor, particulates exhibit a broadband effect on the solar irradiance as a function of wavelength.

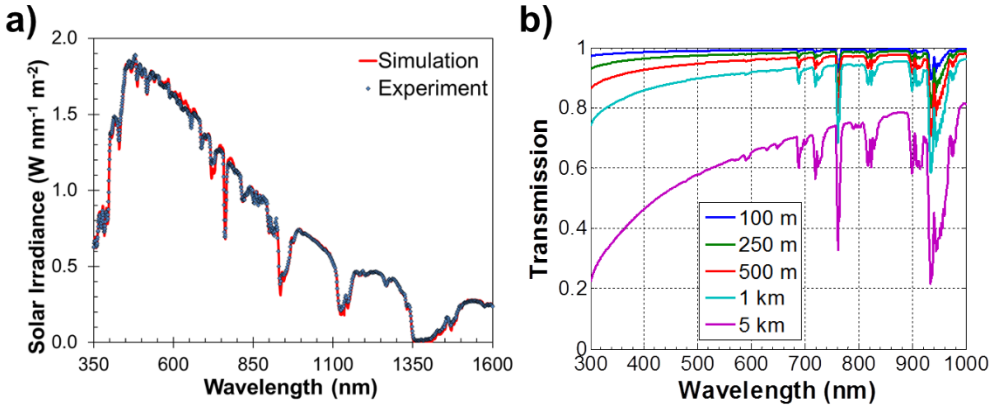

Figure 10: MODTRAN simulations for optical transport in Albuquerque, NM.
a) An example comparison of experimental results and MODTRAN predictions for the solar spectral irradiance for noon on 9/23/2013. b) Calculated optical transmission as a function of wavelength and range.

These methods for determining atmospheric transport contribute to an overall evaluation of how the performance and detection limits of optical radiation detection might vary under different atmospheric conditions. The procedure described above for evaluating spectral transmission is powerful, but it requires a solar tracking spectrometer for the full spectrum optimization, and these specialized instruments are only available at a few locations. Thus, we developed a technique for using published atmospheric data from AERONET (aerosol measurement network), MODIS (Earth-observing satellite) and ASOS (airport weather) stations to determine the local visibility at UV-Visible-NIR wavelengths. These data sources can be used to calculate the optical properties at a wide range of locations, and the data are reported on a daily basis. The procedure for calculating the spectral transmission as a function of wavelength using these data sources is presented in the appendix.

2.8 Outdoor ODR of Charged Particles – Background Characterization

While the COTS camera lenses described in Section 2.5 are excellent for close in testing, remote measurement of the ODR phenomenon requires a more substantial instrument. A custom 'pathfinder' ODR system was built based on a modified 14" Celestron CGE Pro 1400 Schmidt-Cassegrain telescope for a Remote Optical Sensing of Ionizing Radiation (ROSIR) application. The optical path was modified by removing the Schmidt plate, adding custom optical elements to bring the beam out the front and then focus the rays through a computer-controlled filter wheel and on to the CCD detector of the Princeton Instruments camera. Although nominally designed for a 1 km range, the focal position imaged could be adjusted by moving the camera relative to

the final lens in the system using a computerized stage. The ROSIR 'pathfinder' system is shown in Figure 11.

Figure 11: Photograph of the completed ROSIR 'pathfinder' telescope.

We conducted a set of outdoor measurements to evaluate the background UV signal levels that would contribute to the ambient noise. Limited data is available on the ambient UV intensities outdoors, especially at night[5], which will depend on the lunar phase, presence of manmade light sources, weather and atmospheric conditions. Thus, it was necessary to evaluate the background signals under various conditions to ascertain necessary signal levels for detection. We focused early outdoor testing efforts on the acquisition and analysis of experimental field testing using the pathfinder ODR telescope system. Specifically, we investigated the low-level UV-optical backgrounds present in outdoor conditions using the ROSIR pathfinder system under day, night, dawn and dusk conditions as a function of pointing direction while using multiple narrow-band optical filters.

First, we found that the daytime diffuse scattered UV irradiance is more than 6 orders of magnitude more intense than at night (see Figure 12). The intense daytime UV background currently limits the ODR concept to night-time operation, as even the shot noise on the diffuse scattered solar UV content would overwhelm our signal of interest in most cases. Thus, it is of special interest to identify the delimiting boundaries for when ODR measurements are feasible.

Four different times are commonly reported for the transition between night and day, namely sunrise (or set), and civil, nautical and astronomical, nautical twilights; the twilights correspond to the times when the sun is 6, 12, 18 degrees below the horizon, respectively. Figure 12 presents our measured results for the UV diffuse irradiance as a function of time for two narrow band filters (Chroma, 10 nm bandpass, 90% transmission efficiency) covering the two principle nitrogen fluorescence emission lines at 337 and 358 nm. The signals indicate that the nautical twilight is the clear boundary for when the scattered solar intensity begins to rise,

providing a clear limit for when night testing can be accomplished. Similar results were also observed for the day to night transition.

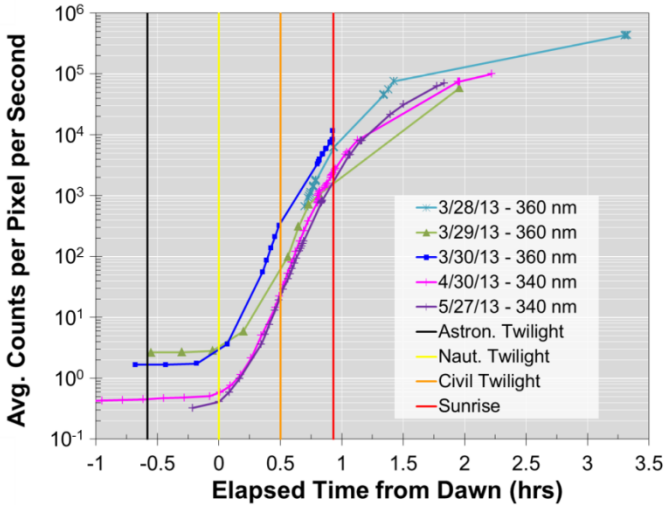

Figure 12: Optical transition from night to day at dawn for several different days.
The signal is shown in the average background intensity for each of the UV bands tested.

The UV background from man-made sources can be greater than from lunar, stellar and other natural sources. City lights contribute to the background sky glow, but lighting fixtures within a few hundred meters of the target can contribute even more significantly to the measured background through scattering. We thus investigated the UV content of man-made lighting. We found that there is a complicated spectral dependence of the emitted intensity as a function of the wavelength, and that there are wide variations in the spectral intensity curves for different brands and models of lights even within the same lighting type[21]. Figure 13a shows these results for a few examples of common outdoor man-made light fixtures. These wide variations preclude the use of a background reduction approach based on the identification of lamp type and spectral subtraction of the UV contributions corresponding to man-made light.

In practice, we observed that the man-made light UV spectral content tends to fall with decreasing wavelength. Figure 13b shows the top of a metal power pole at a distance of approximately 250 meters as a function of time of day and wavelength. During the daytime, the post shows up dark in comparison with the background because the sky is lit by solar scattering for both 360 nm and 340 nm wavelengths. At night, however, the post shows up bright before and after moonrise in comparison to the background for the 360 nm band, indicating the presence of reflected man-made light. For the 340 nm band, the post cannot be seen before moonrise, and shows up dark in comparison to the sky after moonrise. These results suggest that the man-made light content is substantially reduced in the 340 nm band in comparison to the 360 nm band for this scene. It should also be noted that the average intensity in the dark post region of the after moonrise, 340 nm image is actually larger than the average intensity in the same region of the pre-moonrise image.

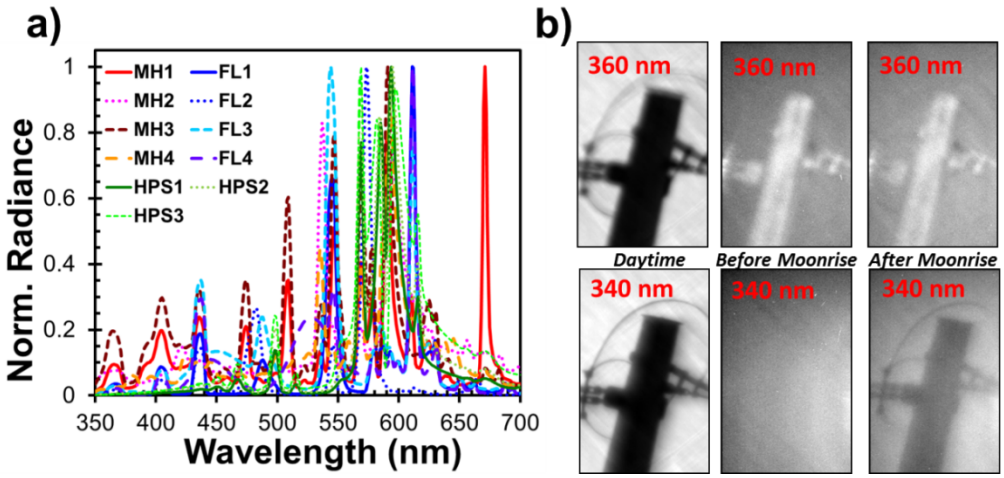

Figure 13: Spectral content of outdoor man-made lamp fixtures.
a) Relative spectral intensity for various outdoor lighting sources (data from Ref. 21), including metal halide (MH), fluorescent (FL) and high-pressure sodium (HPS). b) Detected UV images from the top of a metal power pole under day, pre-moonrise and post-moonrise conditions for 340 and 360 nm wavelength bands.

Given that a spectral subtraction approach for reducing optical backgrounds may not work, we considered a temporal subtraction procedure. In this case, we used the ROSIR pathfinder to directly image an outdoor light at a distance of approximately 120 meters. To evaluate the frequency response of the detected light, we created a bin that included the light and averaged the intensity values for the signal within the bin. Then, we used multiple independent numerical methods written in Matlab to fit the sinusoidal response and extract the frequency (Figure 14).

The frequency analysis showed that fast frame rates could be used to detect the characteristic 'flicker' of man-made sources caused by the AC power flow at relatively long ranges. This time-varying signal could be fit with a sinusoidal curve that could be subtracted out, leaving only steady-state emission which could correspond to a radioactive source. However, this flicker was only found close to manmade light sources, and the low signal obtained away from light sources precludes the use of this technique in many cases.

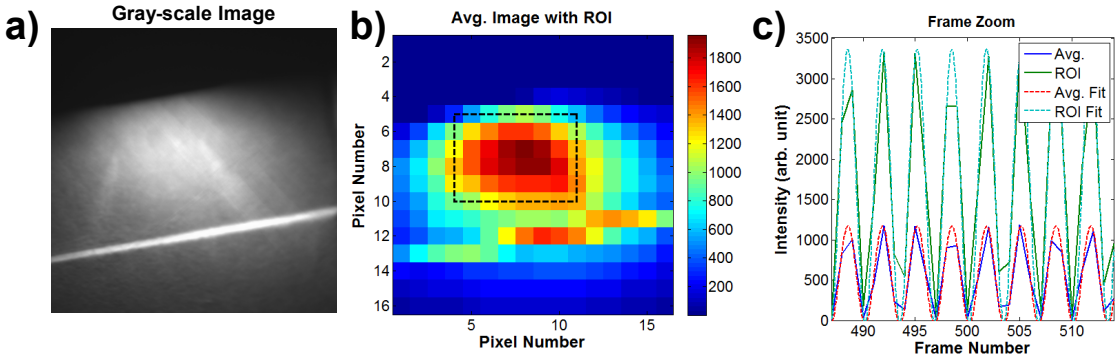

Figure 14: Frequency analysis of an outdoor area illumination lamp.
a) Gray-scale image of the shaded lamp. b) Binned, false-color intensity image. c) Numerical fit of the sinusoidal signal.

Determining the amount of signal corresponding to man-made lighting is vital for the design and detection of radiation-induced air fluorescence in outdoor conditions. The measurements reported here address the issue of identifying and characterizing applicable sources of outdoor optical backgrounds, but more work is still needed to obtain a predictive capability. These background measurements have shown that high backgrounds will be the limiting factor for the outdoor optical detection of radiation and that new approaches for reducing or subtracting the background are needed to improve the SNR and detection limits.

2.9 Outdoor ODR of Charged Particles – Experimental Results

The principal goal of the efforts to measure nitrogen fluorescence is for the real-world field detection of radioactive materials. Previous iterations of optical radiation detection techniques have avoided the significant detection challenges associated with high background outdoor conditions, but dealing with these challenges is necessary for proving optical radiation detection for nuclear forensics applications. Initial attempts to measure nitrogen fluorescence showed that the reflection of ambient lights by the metal enclosure of the ^{210}Po radiation source could be a significant source of interference in detecting the relatively weak signal from nitrogen fluorescence caused by ionizing radiation. Repeated measurements using the pathfinder telescope system equipped with a 360 nm narrow band filter over four consecutive nights revealed that the fluorescence emission light could be distinguished from reflected light using the spatial profile of detected intensity for imaging an alpha emitter. Figure 15a shows the alpha source lit with a UV light emitting diode (LED) and imaged with the telescope system. Figure 15b shows the nitrogen fluorescence from the alpha radiation detected with a 2 hour exposure. The measurements were taken at a distance of 15 meters (500 times the range of the alphas in air) under significant man-made background conditions. The net background subtracted signal shown in Figure 15b was median filtered with a radius of two pixels.

Interestingly, the observed intensity profile in the source signal (Figure 15c) showed maxima between the guard bars, which show up as peaks in the LED-lit profile, and minima behind the guard bars, as was observed in the indoor lab testing (Figure 2). The detected radiofluorescence profile can be compared with the reflection from the LED light. The peaks in the LED lit image correspond to reflections from the guard bars on the source enclosure; these peaks directly overlay the regions of reduced nitrogen fluorescence intensity resulting from radiation shielding and optical blocking.

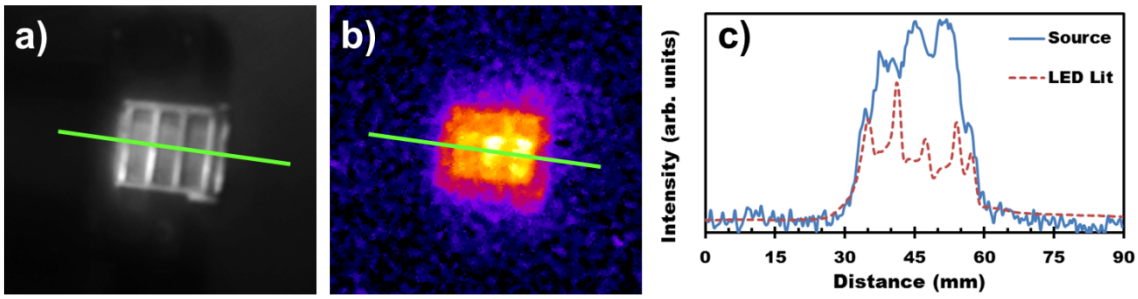

Figure 15: Outdoor measurements of nitrogen fluorescence from a ^{210}Po source.
a) UV LED lit image of the alpha source. b) Two hour exposure, false color image of the radiation dose profile from a head-on view of the alpha-induced fluorescence. c): The line profile of the detected signal corresponding to the green lines in a) and b).

We also observed a dependence on source activity in the observed fluorescence signal intensity by imaging two ^{210}Po alpha sources simultaneously using 10 nm wide bandpass filters (Figure 16, comparable to Figure 7 except under outdoor conditions at >10 times the range). These sources were identical except in their activity, which can be clearly seen as the difference between the intensities around the sources in Figure 16. We performed these measurements using narrow interference filters centered at 360 nm (left) and 340 nm bandpass filter (right).

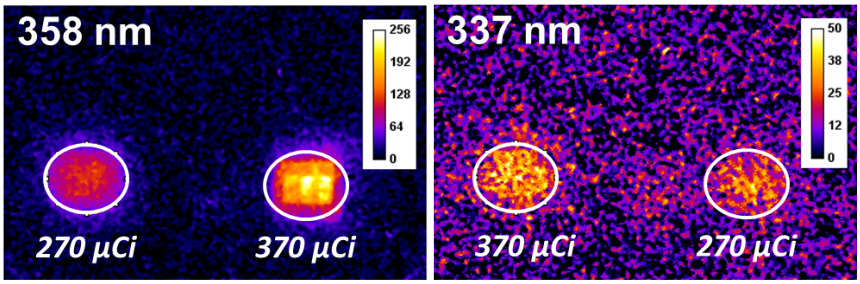

Figure 16: Nitrogen fluorescence images obtained using two different narrowband filters. *The sources were switched between images to validate activity-intensity dependence. The color scales indicate background subtracted optical counts for the exposures.*

A factor of approximately five was observed for the relative signal intensities between the images taken with the 360 and 340 nm bandpass filters for the same exposure time. Given the relative nitrogen yields previously shown in Figure 1 (5.7 ph/MeV @ 337 nm, 3.9 ph/MeV @ 358 nm), and the relative quantum efficiencies of the CCD for the two bands (50% @ 337 nm, 64% @ 358 nm), we would have expected the 340 nm band to have detected 13% brighter signals than the 360 nm band. However, the reflectivity of the COTS primary mirror for the telescope drops precipitously with wavelength in the UV, causing significant reduction in the optical signal collection within the 340 nm wavelength band.

These demonstrations of optical radiation detection outdoors in the presence of significant man-made background light conditions provided a promising verification of the technical approach and showed that the detected fluorescence could be correlated with the relative ionizing energy deposition rates. A comparison of these nitrogen fluorescence images suggests a new multispectral correlation imaging technique for SNR improvement where the calibrated ratios of emission lines from nitrogen fluorescence could be used to uniquely identify air ionization. This approach will be considered for future testing. Future instrument development will focus on improving the detection efficiency at the shorter emission wavelengths, which could be accomplished through the use of a custom coating to enhance the reflectivity of the primary telescope mirror in the UV.

2.10 Indoor ODR of Gamma Rays

A primary accomplishment of this project was to demonstrate the usage of the ODR technique to image the gamma ray radiation dose profile in air from a radioactive source, which is the first demonstration of its kind to our knowledge. Neutral particle radiation sources emitting neutrons or gamma rays are much more difficult to detect via optical dose imaging because of the orders-of-magnitude decrease in the linear energy transfer to air for these radiation types in comparison with charged particles like alphas or betas. However, a credible RDD threat could

consist of gamma sources like cobalt-60 (Co-60) or cesium-137 (Cs-137), so being able to detect this radiation type would represent a major step forward for applying this technique to real nuclear forensics challenges. To explore the optical detection of gamma radiation, we used Sandia National Laboratories' Gamma Irradiation Facility (GIF). This facility operates with sealed-source pins encased in stainless steel cylinders. The sources are stored under 20 feet of water when not in use, but can be raised by elevator for irradiations within a shielded test cell. The steel cladding around the Co-60 pins serves to shield the beta particles emitted, leaving a pure gamma emission with two photons at 1.17 and 1.33 MeV per decay. The GIF was designed for radiation damage testing, but for our purposes served as a high-dose gamma facility for radiation-induced nitrogen fluorescence imaging. At the time of testing, the facility had approximately 220 kCi held in a linear array of pins, and 180 Ci in a single pin.

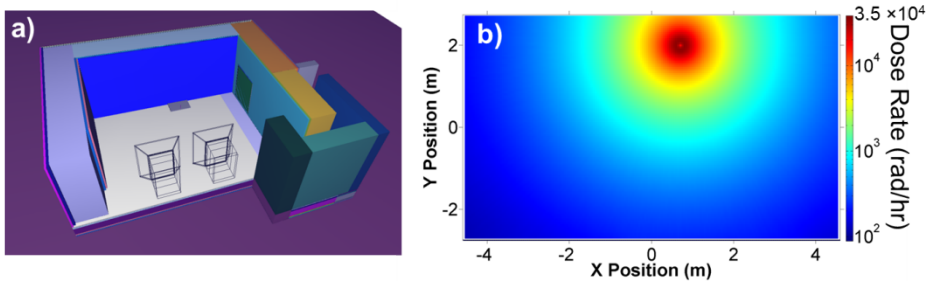

Figure 17: MCNP modeling of the GIF test cell.
a) A cutaway view of the simulated geometry. b) A top-down view of the radiation field parallel to the ground. The logarithmic color scale in b) shows the dose rate (rad/hr) calculated within the test cell for a single pin Co-60 source.

To evaluate expected radiation dose rates and optical signal levels, we modified an existing Monte Carlo N-Particle (MCNP) input deck for our designed experiment. We performed MCNP energy deposition mesh calculations for the test cell (Figure 17). We also developed a custom Matlab script to read in the data generated in the mesh tally, scale to a desired source activity, and then calculate the detectable optical emission along a given optical path.

The pathfinder ODR telescope system is too large to use in the tight spaces within the GIF test cell, so we employed compact optical systems with high UV throughput using components identified in Section 2.6. Specifically, we fielded two instruments for simultaneous data acquisition. The first system utilized a high-zoom Tamron 500 mm *f*/8 catadioptric lens with a 3 inch aperture coupled to the Princeton Instruments ProEM camera. The second system used a wide field 105 mm Nikon UV Nikkor lens with a 1 inch front aperture, which we coupled to a back-illuminated Andor iKon-M 934 scientific camera. The Andor camera has flat quantum efficiency in the UV of ~60 percent down to 300 nm, and can be cooled to -100° C for ultra-low thermal noise on the CCD chip.

We employed a 'folded path' imaging approach for these tests, where there is no direct line of sight from the radiation source to the camera, to minimize the radiation dose to the cameras. In this case, the UV photons emitted from a radiation-excited region were guided by mirrors around corners to image the high-dose region within the cell from a low dose location at the entrance to the maze (Figure 18). The first, smaller mirror for both optical systems was custom-coated with ~99% UV reflectivity (coating by OPCO, λ/10 silica substrate by Edmunds Optics), but the subsequent three were large COTS commercial/residential-grade mirrors. Large

optical-grade mirrors (~1 meter) necessary to achieve the desired field-of-view are cost-prohibitive. The residential-grade mirrors we employed are typically constructed of aluminum or silver metal evaporated onto the back of a glass substrate. We characterized the mirrors and found a reflectivity of ~50% in the 340 and 360 nm bands in the ultraviolet (Figure 18d), which was acceptable for this proof-of-concept experiment.

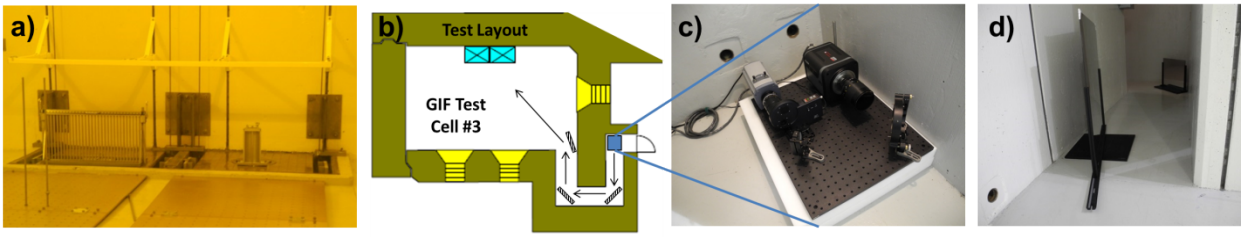

Figure 18: Experimental setup for GIF tests.
a) Photograph through a leaded glass/oil window of raised linear array (left) and single pin (right) Co-60 sources, b) Test cell schematic with optical path identified, c) Photograph of camera setups, and d) Photograph of the mirrors in the maze.

The tests proceeded by taking a white light image with the room lights on, then a background image with all lights extinguished, then another image with the lights off but with the sources raised (signal). This process was repeated for both fielded camera and lens systems and for various exposure times and filtering conditions. A typical example set of these images is shown in Figure 19. The grayscale images shown in Figure 19b and Figure 19c have notably different scales, demonstrating the much higher optical intensity observed in the signal in comparison with the background.

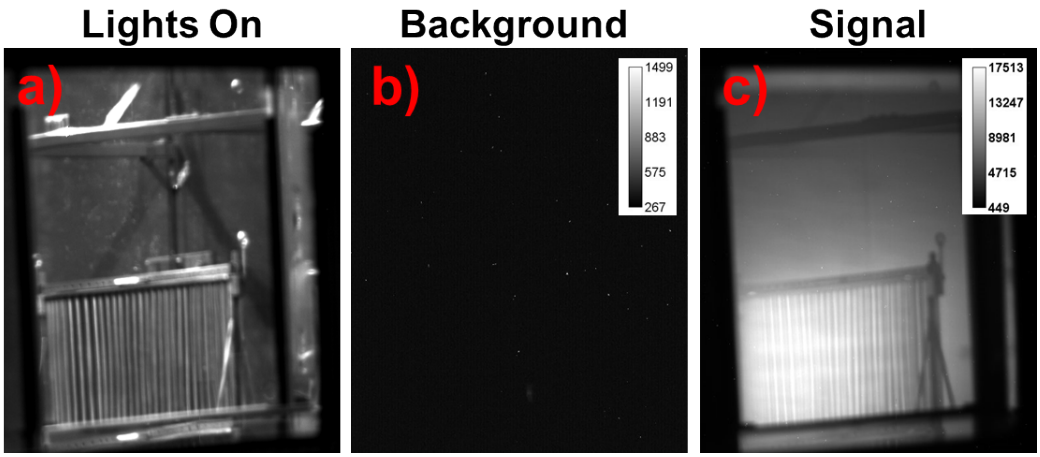

Figure 19: Wide field of view experimental images of the GIF radiation cell.
a) An image of the linear array with the room lights on to identify the target location, b) Background image of the room with the pins down and the pool covered, and c) Radiation-induced fluorescence from gamma dose in air.

The results of our indoor optical gamma detection campaign were immediately conclusive: high radiation fields (10^6 rad/hr) could be imaged from a 6×10^{-3} rad/hr location using the UV-filtered imaging systems. The radiation from the linear array could be detected in as little

as three seconds with the 1-inch aperture UV Nikkor lens and Andor camera system. One unexpected finding was that the Cherenkov optical emission[a] from the linear array stored under the water overwhelmed the UV emission of the single pin. Thus, the pool was covered when taking background images, although this effect is not expected to be an issue for most applications of the ODR technique. Another interesting feature of the experiments was that direct X-ray/gamma strikes on the camera could be detected as single pixel events. These events could be easily filtered out of the final images, but the cameras were kept shielded for most of the tests. We also found that image interpretation can be non-intuitive for volumetric light source such as we see here. Typically, human vision works by looking at reflection from surfaces, but in this case we are integrating the fluorescence emission along the path of the focal length of the system. Figure 20 shows the intensity profile of the signal to illustrate this issue.

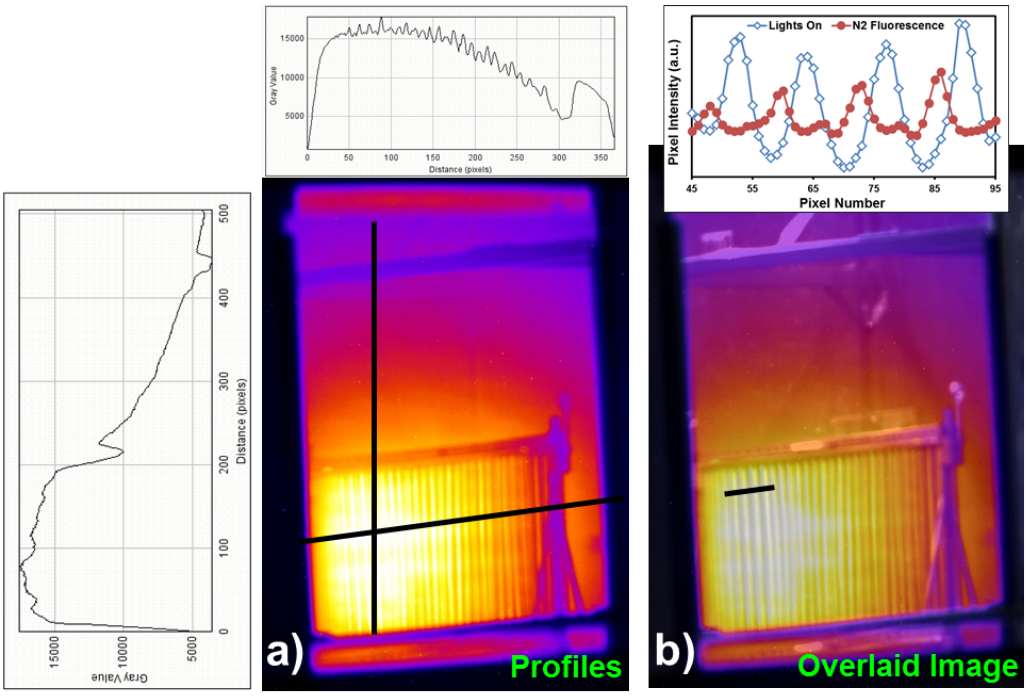

Figure 20: Variation in the UV signal as a function of position.
a) Line intensity profiles across and above the linear array, and b) False color overlaid image of signal intensity on white light room image of the linear array.

These results also open the possibility of employing this technique for the potential application of radiation facility dose mapping, which could be used online to provide more detailed information than existing approaches. The current method for dose rate mapping is a time-consuming task whereby dozens of thermoluminescent dosimeters (TLDs) are placed, irradiated, read out and interpolated between to determine dose rates in the test cell as a function of position. Here, we propose that the optical image resulting from nitrogen fluorescence could be used to image and map the radiation dose rate in the chamber all at once. We believe that this

[a] Cherenkov optical emission from the interaction of relativistic charged particles with dielectric media increases as the wavelength decreases in the UV range. The well-known blue color that we perceive surrounding reactor cores occurs because of a convolution of the spectral emission intensity and eye response as a function of wavelength.

idea has potential to improve the resolution and speed for performing on-line dosimetry for these facilities because of the potentially low optical backgrounds and high radiation dose rates. These results conclusively show that ODR is a feasible technique for imaging gamma radiation in air.

2.11 Outdoor ODR of Gamma Rays

The GIF tests proved that it is possible to detect the optical fluorescence of nitrogen in air induced by high activity gamma sources in controlled conditions. The next goal was to show the promise of this technique in an outdoor environment at standoff ranges, which are conditions relevant to application of this technique for nuclear forensics purposes. To accomplish this goal, we designed an experiment to open an optical path from the outdoors through the 6' thick concrete shield wall and into the GIF radiation test cell. This experiment was possible because of the existence of 10" diameter manipulator ports that pierce the shielding wall. Two locations were available to set up the optical detection instruments: namely, Location 1 at 50 m, and Location 2 at 75 meters from the test cell. Figure 21 shows the test layout for the experiments. The total source activity was reduced to 110 kCi to meet the administrative safety controls, which were verified every time the sources were raised. With this test configuration, the dose was almost negligible (below 1 mrad/hr) at the facility boundary, shown as the 2nd fence in Figure 21.

Two optical instruments were fielded on a mobile truck-based platform with generator power for the computers and cameras. The first instrument was an improved version of the 14" diameter ROSIR 'pathfinder' telescope, with a new black-box camera enclosure and custom-coated high reflectivity turning mirrors and lenses. The second instrument was a tripod-mounted compact camera system with the 3" diameter Tamron lens and a broadband UV filter and the Andor camera. The instruments were aligned with the open port to maximize the field of view through the duct at each of the test locations. The experiments were completed after nautical twilight at night without the complication of the moon (*e.g.* new moon, before moonrise or after moonset), as we had explored in our measurements of the outdoor background intensity (Section 2.8). Typically, a background image acquisition was performed with the sources down, representing a negligible radiation dose in the cell, and then a subsequent image was taken with the sources up. In all experiments, the pool was covered with a thin plastic tarp (optically opaque, but transparent to gammas) to minimize the effect of the Cherenkov illumination in such a way that the cover did not interfere with raising the sources.

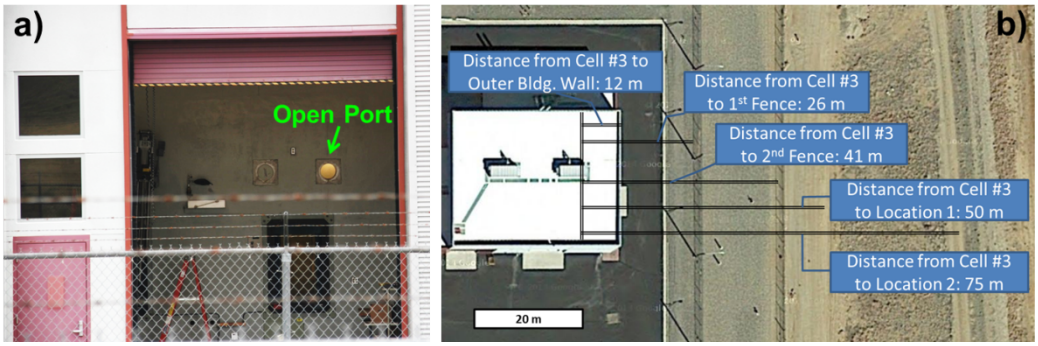

Figure 21: Outdoor optical gamma radiation detection test setup.

a) Photograph of the GIF test cell through an open roll-up door on the east side of the building. The right port above the window is open in this image with the interior lights on, and b) Satellite map of local area with distances from the test cell to important positions.

The outdoor standoff optical radiation detection experiments were successful from the first exposure. The presence of nitrogen fluorescence could be detected through the open port in less than 30 seconds at both locations. Figure 22 shows the results of a typical set of images for each of the two fielded instruments at Location 2.

In these tests, we were able to easily detect the high radiation region within the test cell, even though the ports are approximately ten feet above and ten feet north of the ^{60}Co sources when they are raised into the air in the test cell. This means that that there was not a direct line of sight to the sources, and that any radiation escaping the cell is multiply scattered. We characterized the radiation at Test Location 2, and found a dose rate of 0.2 mrad/hr with a Compton continuum from scattered gammas. At longer ranges, the radiation is theorized to be undetectable using conventional detectors, but still observable with ODR. Although our calculations had predicted that the radiation-induced UV fluorescence at this distance should be detectable, the success of these experiments surpassed our hopes for the signal-to-noise ratio, radiation dose image quality, and requisite exposure times. To validate our initial findings, we ran multiple tests and controlled all sources of light to ensure that all optical conditions were kept identical for the background and 'source up' images.

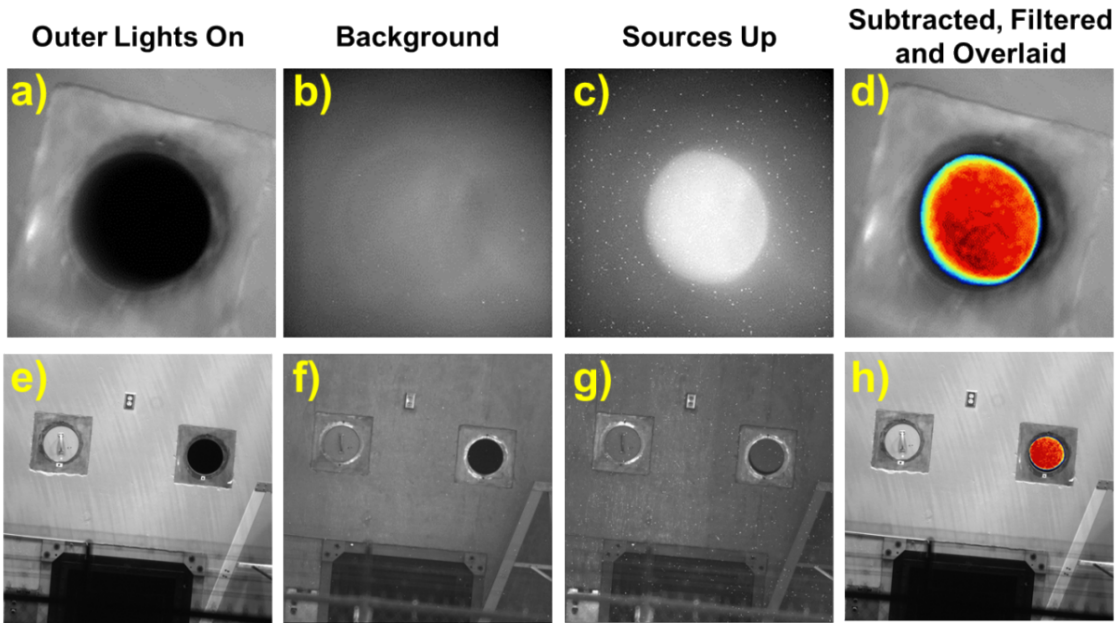

Figure 22: Outdoor optical gamma radiation detection results.
Images a) through d) were obtained with the ROSIR 'pathfinder' telescope, and e) through h) were taken with the compact camera system. a) and e) show the scene with the room lights illuminated, where these UV images can be matched with the visible photograph in Figure 21a. Images b) and f) show the dark background condition, where f) is brighter because of the wider band filter. Images c) and g) show the detected UV signal with the linear array sources up, and should be compared directly to b) and f). Finally, images d) and h) show the background-subtracted images overlaid on the 'room lights' images in a) and e).

In these tests, we were able to easily detect the high radiation region within the test cell, even though the ports are approximately ten feet above and ten feet north of the ^{60}Co sources when they are raised into the air in the test cell. This means that that there was not a direct line of sight to the sources, and that any radiation escaping the cell is multiply scattered. We characterized the radiation at Test Location 2, and found a dose rate of 0.2 mrad/hr with a Compton continuum from scattered gammas. At longer ranges, the radiation is theorized to be undetectable using conventional detectors, but still observable with ODR. Although our calculations had predicted that the radiation-induced UV fluorescence at this distance should be detectable, the success of these experiments surpassed our hopes for the signal-to-noise ratio, radiation dose image quality, and requisite exposure times. To validate our initial findings, we ran multiple tests and controlled all sources of light to ensure that all optical conditions were kept identical for the background and 'source up' images.

We also revisited our multispectral approach to confirm that the light collected matched the emission spectra of the nitrogen fluorescence when normalized according to the pathfinder system efficiency as a function of wavelength. Figure 23 shows some of the results of these tests. The images presented in Figure 23 were useful in validating the experiment, but the relative collection efficiency of the telescope must be considered when comparing the image intensities in terms of counts per second (cps) of signal for the different narrow bandpass filters. The telescope primary reflecting mirror and Princeton Instruments camera have a high efficiency at wavelengths of 400 nm and above, but that efficiency drops sharply and monotonically for shorter wavelengths further into the UV. This explains the relative intensity differences between the 340, 360 and 390 nm filters. We estimate a total system efficiency of 60% for the 390 nm band, compared with 30% for the 360 nm band and less than 10% for the 340 nm band. However, the most important result among these spectral measurements is the lack of signal in the 370 nm band, which would not be expected for natural or man-made optical backgrounds, but should be low for nitrogen fluorescence in comparison with the 360 and 390 nm images.

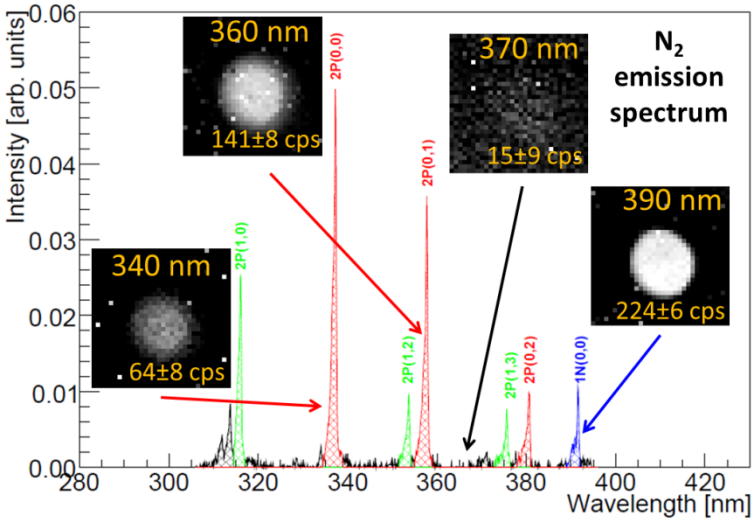

Figure 23: The nitrogen emission spectrum and multispectral ODR images.
The spectrum shows the optical emission bands and intensities of the nitrogen fluorescence at atmospheric pressures. The overlaid images were acquired using different narrow band filters, with arrows to the corresponding emission peaks and the detected signal within the port indicated in counts per second. The center wavelength of each filter is also given on the images.

The success of these multispectral tests was compelling, and thus for our final set of tests in the campaign we attempted to address a 'stretch' goal: detecting a single pin, low activity 150 Ci source pin. This source is at the low end of activity considered a credible RDD threat by the International Atomic Energy Agency (IAEA). Detecting such a low activity source in such non-ideal conditions, where the optical path is limited by the narrow duct and the test cell dimensions, would represent a great step towards addressing nuclear security challenges. As was described in Section 2.5, the signal-to-noise and required exposure times are inversely correlated with the pixel binning, where many pixels are effectively treated as a single collection area. To detect the single pin, we investigated the effect of image size in pixels on the image quality and signal-to-noise ratio for this relatively low activity source. The images presented in Figure 24 show that the lower level activity pin could be at least qualitatively detected from range (Location 2, 75 meters) with a one hour exposure, and that the signal matched expected trends.

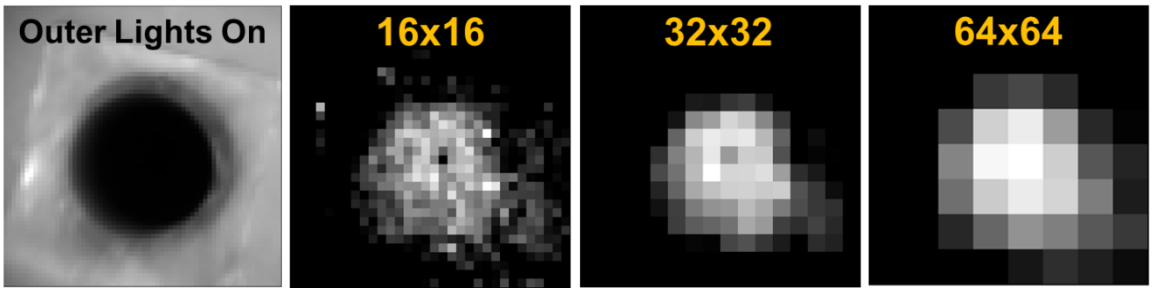

Figure 24: Optical radiation detection as a function of bin size in pixels.
The image on the left shows the scene with the room lights on, where the dark central region is the duct to the test cell. The three images on the right show background-subtracted, thresholded and binned signals for a one hour exposure with a 150 Ci ^{60}Co pin at 75 m, with the bin sizes in pixels shown at the top.

2.12 Next Steps in the Optical Detection of Radiation

The fundamental limitation of the ODR technique in outdoor conditions is high background noise, which limits the technique's current implementation to night-time operation with low manmade lighting. To expand the potential applicability of this technique and overcome current technological limitations, new approaches should be considered. First, we designed a new 'demonstrator' optical radiation detection telescope that will enable optical detection at km-scale ranges. One major improvement in this design is a primary mirror with very high (>95%) and uniform reflectivity from 300 to 400 nm, which would dramatically improve the signal for the lower background, higher emission intensity lines. We also commissioned a custom UV filter with a 50% narrower passband for further reducing the background. Another potential approach could utilize a dual band 340/360 nm filter to specifically capture both of the highest intensity emission lines.

Alternatively, radical new concepts for background reduction could be investigated, including the use of narrowband UV tunable optical filters[b]. A tunable filter with sub-nanometer pass-band width could be used to generate hyperspectral images to provide a 'fingerprint' for the

[b] This effort is currently funded by a NA-22 SBIR based on a topic identified in this work.

presence of ionizing radiation. We also developed a concept to use of inelastic scatter from active laser probing to improve the detection limits of this technique and potentially enable daytime operation. Nitrogen is a very inefficient scintillator, with only 0.007% of deposited radiation energy converted to emitted UV photons. Thus, a significant fraction of the excited states caused by deposited energy from radiation that decay non-radiatively. Active laser probing could dramatically reduce the effect of ambient noise through lock-in amplification and short-time windowing. Figure 25 shows a cartoon of an experimental setup we designed to test the laser probing proof-of-concept experiment.

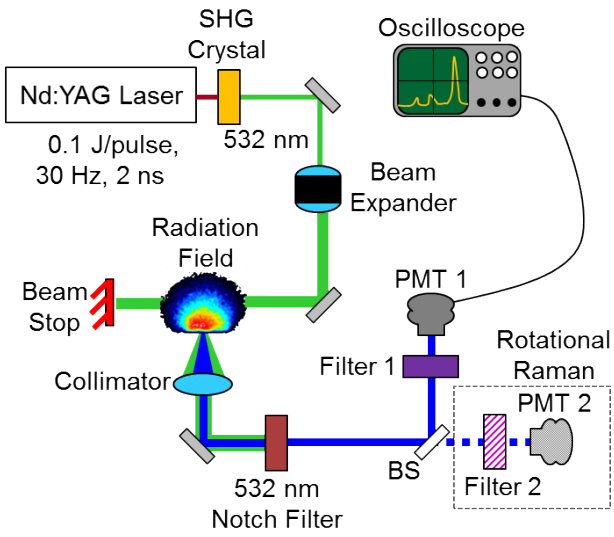

Figure 25: Optical schematic for a proposed Raman LIDAR ODR method.
The designed experiment would employ for laser probing of vibrational and rotational radiation-excited nitrogen molecular states using narrow-band filters.

This idea is related to the Raman Light Detection and Ranging (Raman LIDAR) method, where the spectral content of the backscattered light from a laser pulse is typically measured to detect chemicals from a distance. In our concept, the Raman scattering from nitrogen molecules in the atmosphere could be used to detect radiation fields remotely by measuring non-equilibrium rotational and vibrational population levels. A pulsed LIDAR method could also provide a distance-dependent measure of radiation from the return time signal. A review of the scientific literature identified several analogous techniques that provide promising indication for the viability of this proposed approach, including the laser-based measurement of ionized nitrogen in aurora[22], the rapid LIDAR measurement of atmospheric temperatures at kilometer scales during the daytime with single degree accuracy[23], and the spontaneous optical anti-Stokes measurement of temperature in a furnace[24].

Finally, we recommend a future project to fully characterize the optical emission and collection to obtain efficiency values as a function of dose. This could be accomplished using optical images, lens characterization, well-characterized sources/radiation facilities, thermoluminescent dosimeters and other sensors to enable quantitative ODR using a well-characterized conversion of UV counts to dose rate.

3. GRAPHENE FIELD EFFECT TRANSISTOR SENSOR

A portion of our efforts were devoted to develop a new kind of radiation sensor utilizing a graphene field effect transistor (GFET) as a sensing element. The GFET research is aimed at developing a new sensor architecture that can improve room temperature resolution over conventional designs. For radiation detection, graphene could act as an ultra-low-noise, ultra-sensitive detector for radiation-induced charges generated in a semiconductor material. This work was performed in conjunction with Steve Howell of Sandia's Radiation Hardened CMOS Technology group.

Graphene is a planar, atomically thin form of carbon with unique electrical and material properties that could enable new high performance radiation detectors. Contrary to common semiconductor radiation detection schemes, a FET detector could be sensitive to a single charge carrier, rather than needing to collect both an electron and hole pair. This unipolar sensitivity could be an important feature for high density, room-temperature semiconductor materials that have been proposed for radiation detectors that suffer from significant hole trapping. Graphene is of specific interest because it can be transferred to any flat material substrates and can be patterned using standard lithography techniques. Graphene can be thought of as a unique zero-bandgap semiconductor (semi-metal) where the cones of the valence band and conduction band meet at the Dirac point (point where the film is charge neutral). A slight electric field applied to the graphene will shift the Fermi level, transitioning from holes to electrons as the preferred charge carrier and leading to significant changes in the conductivity of the material. This 'sharp feature' and high carrier mobilities lead to a material that has strong advantages for charge sensing. Incorporating graphene into a field-effect transistor architecture could provide an extremely high sensitivity readout mechanism for sensing individual charge carriers.

The GFET device structure consists of two electrodes connected to a graphene thin film on top of an insulator on a semiconductor absorber, as shown in Figure 26. With a voltage bias from the back gate electrode and the source/drain electrodes, the charges generated by radiation absorbed in the semiconductor collect underneath the isolating insulator layer. These charges exert an electric field on the graphene layer, modifying the Fermi level and dramatically affecting the film conductivity. This change can be measured by placing the source and drain electrodes at slightly different potentials, and measuring the current flow across the FET. Interestingly, these devices will only effectively collect charges from a depletion layer, where the fields are 'felt' in the semiconductor absorber. This layer thickness will depend on the level of dopants and impurities in the material, which should be kept as low as possible to increase charge collection efficiency, but it will also depend on the applied back gate voltage, which could enable discrimination based on radiation energy or type.

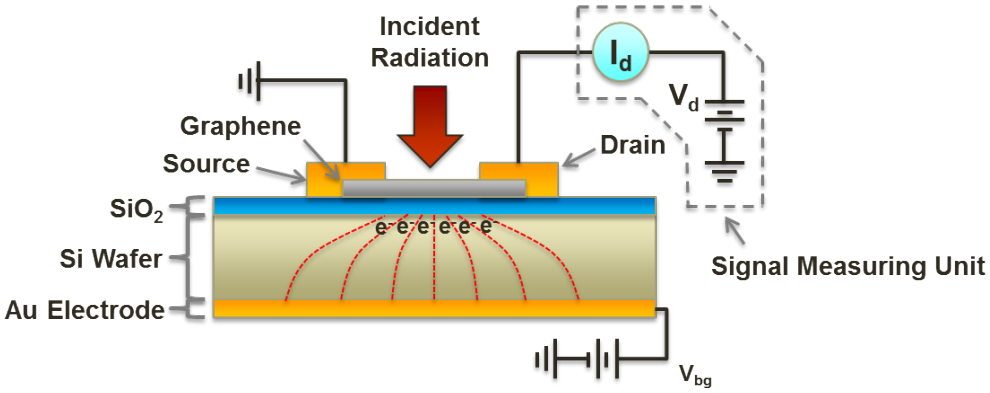

Figure 26: A schematic for the GFET device structure.

We performed a set of experiments to measure the optical response using several GFET devices on silicon and silicon carbide (SiC) substrate materials. Silicon carbide is a wide bandgap semiconductor with low thermal charge generation. These tests provided a direct measure of the ability of the device to collect and accumulate charge beneath the insulator through an effect on the graphene conductivity. No response was observed with or without the incident light when no back gate voltage (V_{bg}) was applied, but a strong change in the current flow is observed with light and an applied field, indicative of a field-effect mechanism (Figure 27). When the light is turned off, the initial current level slowly recovers as collected charges diffuse away from the GFET. The 'Light On' case in Figure 27 shows a strong detector response to optical light. Interestingly, the drop was not linear, but rather asymptotic. The transition to a stable current flow under optical illumination suggests competing mechanisms of charge buildup and electrostatic repulsion or diffusion that result in an eventual equilibrium for a given charge generation rate. Improved quality substrates and dielectric films were also found to speed up this response to the sub-second level.

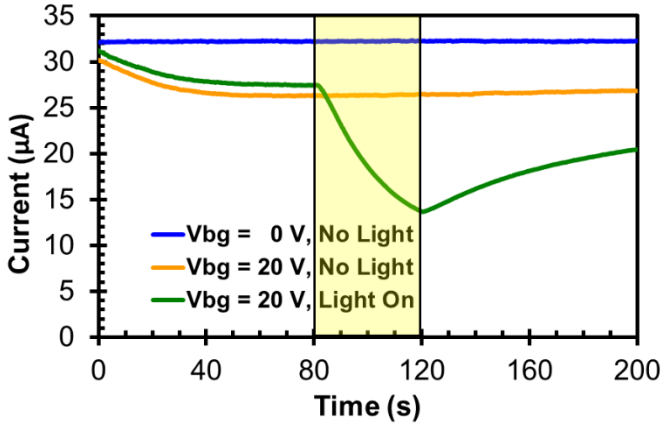

Figure 27: Optical detection using a GFET device fabricated on a SiC substrate.

The next step was to apply the GFET device to the task of radiation detection. For these experiments, we used the ^{210}Po alpha emitter in a top-side irradiation configuration. Our first measurements were made to verify that the single-layer graphene was not damaged by the incident alpha particles, which was verified by measuring the unchanged graphene resistance

before and after irradiation with the source positioned immediately on top of the GFET substrate for 5 minute exposures.

Our tests of the capacity of the GFET devices for radiation detection showed a clear effect on the current flow when exposed to alpha irradiation (Figure 28). As opposed to the case of optical illumination, alpha irradiation led to discrete steps in the current corresponding to the absorption of individual alpha particles. For these substrates, we calculate that only a small fraction of the overall alpha particle energy is deposited in the depletion region where charges can be effectively collected, whereas most of the optical energy is deposited within this layer. Figure 28 shows that the trends and average current change with time is approximately constant for different tests over the same amount of time, but that the instantaneous individual point-to-point current changes are random. We calculate that only a small fraction of the particle energy could be captured in the depletion depth of these initial devices.

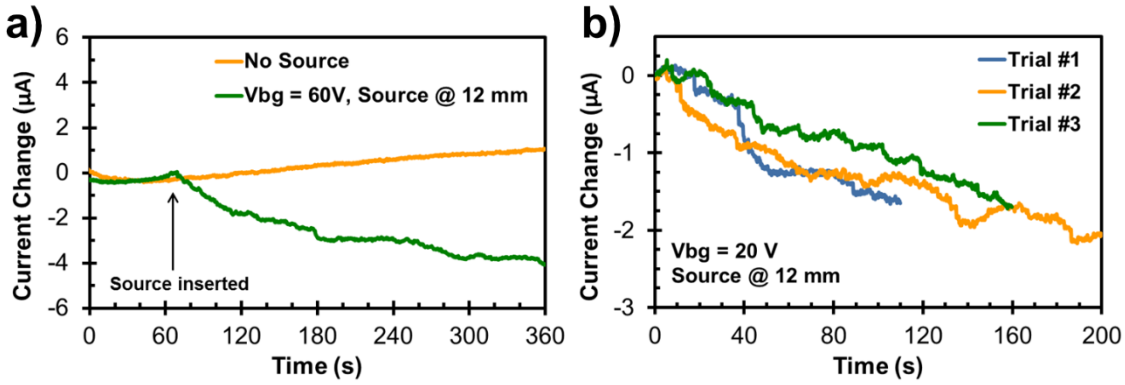

Figure 28: Radiation detection with a GFET device.
a) Comparison of signal changes observed for background and alpha exposure test cases. b) Repeated experiments showing the statistical fluctuations in the detection of charges resulting from the absorption of individual alpha particles.

These initial optical and radiation detection proof-of-concept experiments demonstrated the charge collection and detection capabilities of GFET sensors, and showed the potential of these devices for high sensitivity, high-resolution and single particle detection. These results are described in greater detail in a recent Sandia internal SAND report[25].

Further efforts in this area have focused on identifying and obtaining higher quality materials to improve the performance of the GFET device structure. This effort encompassed all material layers in the device. For example, when the silicon oxide insulator layer, which was initially deposited with plasma-enhanced chemical vapor deposition, was replaced with a thermally grown oxide or atomic layer deposited hafnia oxide (HfO_2), the speed and repeatability of the device improved. We also investigated the use of low dopant, high resistivity silicon for use as a substrate material because of improved carrier transport. Likewise, we pursued specialized substrates like cadmium zinc telluride (CZT) for gamma ray detection and synthetic diamond for charged particles because of their relatively high bandgap (corresponding to low thermally generated charge carriers) and high charge mobility. Lastly, the research included developments towards obtaining very high quality graphene for transfer, which would increase the sensitivity and yield of fabricated devices. Very high quality, large area graphene can be fabricated on the surface of a silicon carbide with a straightforward process, but the material is

challenging to use in this form. The ability to transfer this high quality graphene onto other substrates would enable improved GFET device performance. We investigated a photoelectrochemical etching process to eat through a silicon carbide substrate to free the graphene monolayer for further usage. These experiments were successful, achieving 1.5 µm/hr etch rates from a custom designed UV/optical setup. Another area of active research is the development of a monochromator setup for delivering narrow band light to the GFET device for characterizing the depletion depth and quantum efficiency of the devices as a function of charge generation location. The depletion depth should be considered as the radiation collection region of the substrate. Figure 29 shows a set of calculations of the effect of photon energy on the deposition efficiency in the depletion volumes that can be achieved with current designs. Figure 29 shows that measuring the absorption of different wavelengths of light and corresponding generation of charge carriers as a function of depletion depth of the material for well characterized incident optical powers. This analysis is also important, because it shows that only X-rays will be detectable with the current design, which we believe will only allow for a depletion depth of up to 15 µm. Alternative pathways to deep depletion depths are possible, however, and will be pursued in future work. For comparison, the estimated range for charged particles is also shown in Figure 29c and Figure 29d[16].

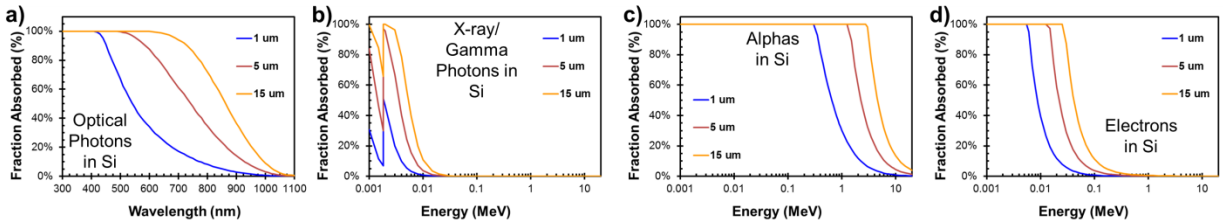

Figure 29: Fraction of radiation energy absorbed deposition in silicon.
The calculations are shown as a function of incident energy and depth for a) optical photons, b) X-ray/gammas, c) alpha particles, and d) electrons.

In the limited time allotted for the research and development of the GFET radiation detector, we proved the technical concept and identified methods for improving fabricated devices. Future work will focus on identifying applications for the technology and demonstrating the achievable energy resolution using a GFET detector.

4. MENTORING

Mentoring is an important component in developing young students into the scientists of the future who can tackle difficult problems affecting our national security. We view mentoring, fostering student development, and outreach as integral parts of our work, both in terms of giving back to the scientific community and in providing an opportunity for students to contribute to our mission while expanding their skill set and exposing them to the field of nuclear forensics. We had the privilege of working with outstanding students in the course of this project. Here we outline the mentoring efforts that occurred under this project and discuss project outcomes.

4.1 2013 Monitoring Systems and Technology Summer Intern

The first summer intern we had the opportunity to work was an Albuquerque high school student, who came in with a passion for robotics and an eager willingness to learn. We served as the student's primary mentor for his ten week Summer 2013 internship. Some of the student's contributions for the summer included developing a CAD model of the optical radiation detection telescope system, investigating automation options for field imaging, and performing measurements of the telescope field of view. Since his summer internship, the student has gone on to attend the University of Arkansas, and returned to Sandia in the Summer of 2015 as an intern in another group.

4.2 2013 NTNFC Undergraduate Scholar

Our second summer intern was a South Carolina State University student and Department of Homeland Security National Technical Nuclear Forensics Center (NTNFC) Undergraduate Scholar. The student worked closely with us in the summer of 2013, and then returned to his home institution to work remotely for the fall semester, with a final presentation of his work presented at the NTNFC Undergraduate Scholars Program culmination meeting December 19th hosted at Sandia. When the student arrived at Sandia, we developed a project to develop techniques for the field detection of fission products that are difficult to measure with conventional collection and lab gamma spectroscopy techniques. Specifically, a sensitive measurement in the field for very short or long-lived isotopes could provide an added capability for nuclear forensics applications. The initial concept to address this need included a ruggedized, inexpensive and fieldable air sampling air pressure spark discharge plasma optical spectroscopy system, analogous to laser-induced breakdown spectroscopy, which would continuously sample airborne particulates to test for elements of interest. During the summer, the student built a spark source and investigated potential optical emission lines of interest for important fission products. Working together, we designed a test system, ordered components and laid out a pathfinder system. Upon his return to college, the student shifted focus and considered an alternative technique for fission product identification, X-ray fluorescence. These seemingly disparate methods could be excited simultaneously by ultrafast laser pulses or in kilovolt potential discharges to provide two orthogonal detection schemes and provide high confidence results. After his internship, the student continued in the NTNFC Undergraduate Fellow program with an internship at Los Alamos National Laboratories investigating microscopy for nuclear forensics applications.

4.3 2014 Monitoring Systems and Technology Summer Intern

During the summer of 2014, we had the opportunity to work with a hand-selected electrical engineering junior from New Mexico State University. The student worked with us on the optical detection of radiation project, where he worked on improving a previously developed code for coupling radiation transport and optical emission/collection, and strongly contributed to the indoor optical radiation detection measurement campaign at the Gamma Irradiation Facility. This particular student excelled in his work ethic and self-motivation, and he was a substantial benefit to the research effort. He has since graduated with dual degrees in Math and Electrical Engineering, and gone on to study optical engineering at one of the premier programs at the University of Arizona.

4.4 2014 NTNFC Undergraduate Scholar

We had the opportunity to work with a George Washington University chemistry student. This student started working with us during the summer of 2014 as a Department of Homeland Security NTNFC Undergraduate Fellow. She worked on developing optical emission spectroscopy techniques for elemental determination for nuclear forensics applications. In our work to advance this technology, we had the opportunity together with a collaborator in another division (Ken Armijo) to characterize the spectral content of plasmas containing various elements. This synergistic work, which helped us develop our capabilities while employing our collaborators' plasma source and providing them with our optical characterization information, was very productive. On our side, we were able to identify emission lines from elements of nuclear forensics interest such as Mo and Sr, and evaluate the effects of plasma temperature by comparing an electrical discharge plasma with a laser-induced breakdown spectroscopy (LIBS) emission lines. For our collaborators, we were able to show changes in plasma optical emission corresponding to increases in plasma temperatures as a function of electrical discharge power, indicate the moment of flame ignition, and identify different elements in electrodes. This work led to our inclusion as authors on two conference proceedings and an accepted peer-reviewed journal article[26]. Through the support of the NTNFC office, we were able to work with this student again in the summer of 2015, where the student delved deeper into the physics of optical emission in support of several nuclear forensics projects around the group. She was able to make an immediate impact, and contributed by independently completing a literature review on spectroscopy techniques and an independent series of tests that will provide data to validate numerical models developed over the course of the summer. This student is beginning graduate study in the Fall of 2015 at University of California at Irvine, where she will study nuclear radiochemistry as a Department of Defense SMART Fellow.

4.5 Outreach

In the course of this project, we had the opportunity to participate in outreach for Sandia's Take Our Daughters and Sons to Work Day and Family Day. In each of the past three years, we led or assisted with experimental demonstrations for kids attending the event. We helped run laser ionization breakdown spectroscopy (LIBS) demonstrations with Curt Mowry of Sandia's Materials Reliability group. In this demonstration, children bring their own rocks and LIBS is used to determine what elements are present in the sample. The demonstration is used to discuss how the Mars Rover has seen similar results for Martian samples. In addition, we worked with Jared Greenwald of Sandia's Phenomenology & Sensor Science group to develop a cloud

chamber setup to show how radiation is all around us and can be detected with ordinary household materials. We also developed and run interactive demonstrations of the use of laser diffraction to measure the thickness of the children's hair, and the use of cameras to show the ability to detect ultraviolet and infrared light outside the visible range using a prism and rainbow. Since converting to staff, we also reached back to the post-doc community at Sandia, serving as a judge for the annual post-doc poster session and a panelist at a work experience seminar. Through these rewarding activities, we had the chance to show how science and careers in nuclear and optical engineering can be fun, exciting and useful.

5. CONCLUSIONS

During the course of this project, we made major strides towards developing technologies to address nuclear forensics challenges. Our research resulted in significant advancements in optical detection of radiation capabilities—which started as an idea when we began this project and advanced through indoor detection of charged-particle induced radiation to our culminating demonstration of gamma radiation though a small window at a distance of 75 meters. Likewise, we proved the concept behind the operation of graphene-based field effect transistor radiation sensors. These major steps forward bring our research closer to relevance for nuclear forensics applications. We sketched out paths forward for improving the capabilities of each of the technologies described in this report. These steps forward have advanced our capabilities to contribute to the nuclear forensics mission.

REFERENCES

1. T. Waldenmaier, "Spectrally resolved Measurement of the Nitrogen Fluorescence Yield in Air induced by Electrons," *Institut für Kernphysik, Universität Karlsruhe Dissertation* (2006).
2. K.-H. Kampert and A.A. Watson, "Extensive Air Showers and Ultra High-Energy Cosmic Rays: A Historical Review," *European Physical Journal H* **37**, 359-412 (2012). DOI: 10.1140/epjh/e2012-30013-x
3. A.N. Bunner, "Cosmic Ray Detection by Atmospheric Fluorescence," *Cornell University Ph.D. Dissertation* (1967).
4. H.E. Bergeson *et al.* "Measurement of Light Emission from Remote Cosmic-Ray Air Showers," *Physical Review Letters* **39**, 847-849 (1977). DOI: 10.1103/PhysRevLett.39.847
5. R.M. Baltrusaitis, R. Cady, G.L. Cassiday, R. Cooper, J.W. Elbert, P.R. Gerhady, S. Ko, E.C. Loh, M. Salamon, D. Steck and P. Sokolsky, "The Utah Fly's Eye Detector," *Nuclear Instruments and Methods in Physics Research A* **240**, 410-428 (1985). DOI: 10.1016/0168-9002(85)90658-8
6. J. Abraham *et al.*, The fluorescence detector of the Pierre Auger Observatory. *Nuclear Instruments and Methods in Physics Research A* **620**, 227-251 (2010). DOI: 10.1016/j.nima.2010.04.023
7. M. Casolino *et al.*, Detecting ultra-high energy cosmic rays from space with unprecedented acceptance: objectives and design of the JEM-EUSO mission. *Astrophysics and Space Sciences Transactions* **7**, 477-482 (2011). DOI: 10.5194/astra-7-477-2011
8. P. Colin, A. Chukanov, V. Grebenyuk, D. Naumov, P. Nedelec, Y. Nefedov, A. Onofre, S. Porokhovoi, B. Sabirov and L. Tkatchev, "Measurement of air and nitrogen fluorescence light yields induced by electron beam for UHECR experiments," *Astroparticle Physics* **27**, 317-325 (2007). DOI: 10.1016/j.astropartphys.2006.11.008
9. J. Rosado, F. Blanco and F. Arqueros, "Comparison of available measurements of the absolute air-fluorescence yield," *Astroparticle Physics* **34**, 164-172 (2010). DOI: 10.1016/j.astropartphys.2010.06.007
10. A.J. Peurrung *et al.,* "Alternative Signatures for Special Nuclear Material Detection," *Pacific Northwest National Laboratories* PNNL-14395 (2003).
11. S.M. Baschenko, "Remote optical detection of alpha particle sources," *Journal of Radiological Protection* **24**, 75-82 (2004). DOI: 10.1088/0952-4746/24/1/006
12. D.L. Chichester and S.M. Watson, "Multispectral UV-Visual Imaging as a Tool for Locating and Assessing Ionizing Radiation in Air," *IEEE Transactions on Nuclear Science* **58**, 0018-9499 (2011). DOI: 10.1109/TNS.2011.2163825
13. J. Sand, S. Ihantola, K. Peräjärvi, A. Nicholl, E. Hrnecek, H. Toivonen and J. Toivonen, "Imaging of alpha emitters in a field environment," *Nuclear Instruments and Methods A* **782**, 13-19 (2015). DOI: 10.1016/j.nima.2015.01.087
14. J.S Feener and W.S. Charlton, "Preliminary Results of Nuclear Fluorescence Imaging of Alpha and Beta Emitting Sources," *ANIMMA 3rd Conference*, Marseille, France (2013).

15. B. Fahimian, A. Ceballos, S. Türkcan, D.S. Kapp and G. Pratx, "Seeing the invisible: Direct visualization of therapeutic radiation beams using air scintillation," *Medical Physics* **41**, 010702 (2014). DOI: 10.1118/1.4851595

16. M.J. Berger, J.S. Coursey, M.A. Zucker, and J. Chang, "ESTAR, PSTAR, and ASTAR: Computer Programs for Calculating Stopping-Power and Range Tables for Electrons, Protons, and Helium Ions (version 1.2.3)," Online, available at http://physics.nist.gov/Star, accessed 3/3/2014, National Institute of Standards and Technology, Gaithersburg, MD (2005).

17. D. Deriso, "Invisible Colors," http://www.nature.com/scitable/blog/the-artful-brain/alternate_realities, Article on The Artful Brain, a blog at Scitable by Nature Education, posted May 22, 2011, Accessed March 27, 2014.

18. K. Schmitt, Weinheim,Germany, http://photographyoftheinvisibleworld.blogspot.com/, Accessed March 27th, 2014.

19. J. Fishman, A.E. Wozniak and J.K. Creilson, "Global distribution of tropospheric ozone from satellite measurements using the empirically corrected tropospheric ozone residual technique: Identification of the regional aspects of air pollution," *Atmospheric Chemistry and Physics* **3**, 893-907 (2003). DOI: 10.5194/acp-3-893-2003

20. K.M. Armijo, R.K. Harrison, J.B. Martin and B.H. King, "Spectral derates phenomena of atmospheric components on multi-junction CPV modules," *Abstract for the 10th International Conference on Concentrator Photovoltaic Systems CPV-10* (2013).

21. C.D. Elvidge, D.M. Keith, B.J. Tuttle and K.E. Baugh, "Spectral Identification of Lighting Type and Character," *Sensors* **10**, 3961-3988 (2010). DOI: 10.3390/s100403961

22. R.L. Collins, L. Su and D. Lummerzheim, "Investigating the Auroral Thermosphere with N_2^+ Lidar," Report from the Geophysical Institute at the University of Alaska Fairbanks (2006).

23. M. Radlach, A. Behrendt and V. Wulfmeyer, "Scanning rotational Raman lidar at 355 nm for the measurement of tropospheric temperature fields," *Atmospheric Chemistry and Physics* **8**, 159-169 (2008). DOI: 10.5194/acp-8-159-2008

24. G. Zikratov, F.-Y. Yueh, J.P. Singh, O.P. Norton, R.A. Kumar and R.L. Cook, "Spontaneous Anti-Stokes Raman Probe for Gas Temperature Measurements in Industrial Furnaces," *Applied Optics* 38, 1467-1475 (1999). DOI: 10.1364/AO.38.001467

25. R.K. Harrison, S.W. Howell, J.B. Martin, A.B. Hamilton, "Exploring Graphene Field Effect Transistor Devices to Improve Spectral Resolution of Semiconductor Radiation Detectors," *Sandia Report* #SAND2013-10104, (December 2013).

26. K.M. Armijo, J. Johnson, R.K. Harrison, K.E. Thomas, M. Hibbs, and A. Fresquez, "Quantifying Photovoltaic Fire Danger Reduction with Arc-Fault Circuit Interrupters," *Progress in Photovoltaics* (2014). doi: 10.1002/pip.2561

27. National Oceanic and Atmospheric Administration, Department of Defense, Federal Aviation Administration, and United States Navy, "Automated Surface Observing System (ASOS) User's Guide," (1998).

28. ftp://ftp.ncdc.noaa.gov/pub/data/asos-onemin/

29. National Climatic Data Center, "Data Documentation for Data Set 6405 (DSI-6405): ASOS Surface 1 Minute Data," Asheville, North Carolina (2006).

30. Blake Lasher, National Oceanic and Atmospheric Administration, personal communication (2015).

31. A. Bucholtz, "Rayleigh-scattering calculations for the terrestrial atmosphere," *Applied Optics* **34**, 2765-2773 (1995). DOI: 10.1364/AO.34.002765.

32. A.L. Kessner, J. Wang, R.C. Levy and P.R. Colarco, "Remote sensing of surface visibility from space: A look at the United States East Coast," *Atmospheric Environment* **81**, 136-147 (2013). DOI: 10.1016/j.atmosenv.2013.08.050.

33. B.N. Holben *et al.*, "An emerging ground-based aerosol climatology: Aerosol Optical Depth from AERONET," *Journal of Geophysical Research* **106**, 12067–12097 (2001). DOI: 10.1029/2001JD900014.

34. C.O. Justice *et al*., "The Moderate Resolution Imaging Spectroradiometer (MODIS): land remote sensing for global change research," *IEEE Transactions on Geoscience and Remote Sensing* **36**, 1228-1249 (1998). DOI: 10.1109/36.701075

35. J.D. Spinhirne, J.A. Reagan and B. M. Herman, "Vertical Distribution of Aerosol Extinction Cross Section and Inference of Aerosol Imaginary Index in the Troposphere by Lidar Technique," *Journal of Applied Meteorology* **19**, 426–438 (1980). DOI: 10.1175/1520-0450(1980)019<0426:VDOAEC>2.0.CO;2.

36. M.J. McGill, D.L. Hlavka, W.D. Hart, E.J. Welton and J. R. Campbell, "Airborne lidar measurements of aerosol optical properties during SAFARI-2000," *Journal of Geophysical Research* **108**, 8493 (2003). DOI: 10.1029/2002JD002370.

37. D. Bäumer, B. Vogel, S. Versick, R. Rinke, O. Möhler and M. Schnaiter, "Relationship of visibility, aerosol optical thickness and aerosol size distribution in an ageing air mass over South-West Germany," *Atmospheric Environment* **42**, 989-998 (2008). DOI: 10.1016/j.atmosenv.2007.10.017.

38. A. Retalis, D.G. Hadjimitsis, S. Michaelides, F. Tymvios, N. Chrysoulakis, C.R.I. Clayton and K. Themistocleous, "Comparison of aerosol optical thickness with *in situ* visibility data over Cyprus," *Natural Hazards and Earth System Sciences* **10**, 421-428 (2010). DOI: 10.5194/nhess-10-421-2010.

39. K.H. Lee, M.S. Wong, K. Kim and S.S. Park, "Analytical approach to estimating aerosol extinction and visibility from satellite observations," *Atmospheric Environment* **91**, 127-136 (2014). DOI: 10.1016/j.atmosenv.2014.03.050.

40. S.M. Raffuse, M.C. McCarthy, K.J. Craig, J.L. DeWinter, L.K. Jumbam, S. Fruin, W.J. Gauderman and F.W. Lurmann, "High-resolution MODIS aerosol retrieval during wildfire events in California for use in exposure assessment," *Journal of Geophysical Research Atmospheres* **118**, 11242-11255 (2013). DOI: 10.1002/jgrd.50862

APPENDIX: VISIBILITY CALCULATIONS FOR UV TRANSPORT

The wavelength-dependent attenuation of light as a function of distance is a crucial parameter for optical sensing applications. The parameter is vital because the optical transport can vary dramatically between different locations, season, and even within a single day. To obtain time-resolved local optical properties, we use the Automated Surface Observing System (ASOS), which is a network of instruments at ~1000 sites at airports across the United States[27] (Figure 30).

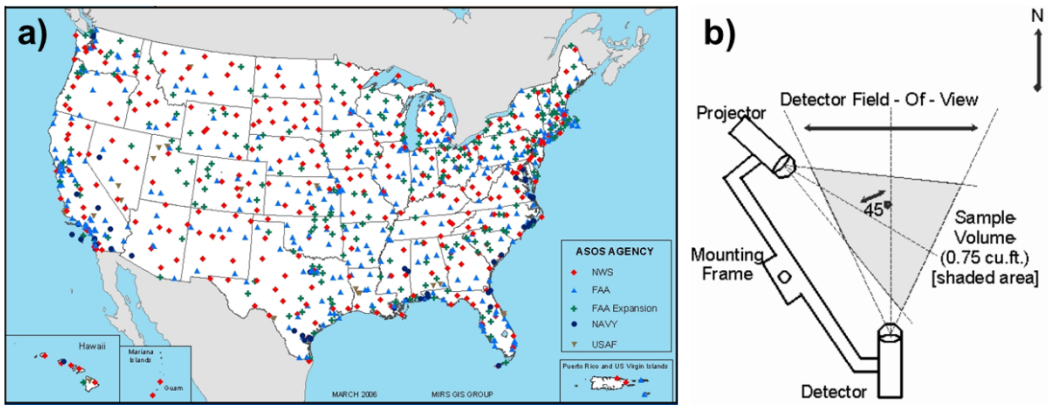

Figure 30: ASOS visibility sensor system characteristics.
a) ASOS sensor locations in the United States, and b) Operating diagram for the forward scatter sensor that is calibrated to provide extinction/visibility output data[1].

The ASOS network was developed through a coordinated effort by the National Oceanic and Atmospheric Administration (NOAA), Department of Defense (DoD) and the Federal Aviation Administration (FAA). The ASOS sites are typically located near population centers and at airports. In addition to sensors such as temperature, pressure, relative humidity, wind velocity, precipitation, and cloud coverage, the ASOS sites also include Belfort Model 6220 forward scatter sensors to determine the visibility. Specifically, the sensor consists of a broadband xenon flashtube transmitter and filtered optical detector that has been calibrated to the optical transmission at 550 nm. The standard ASOS data sets available online only report visibility data up to a visibility of 10 miles, but the raw meteorological measurements provided in the National Climactic Data Center's Data Set 6405[28,29,30] provide the total optical extinction coefficient β_{ext}, including both scattering and absorption, in inverse kilometers at an effective wavelength of 550 nm on a minute-by-minute interval. This data can be related to the visibility V within the high and low attenuation detection limits of the sensor according to the ASOS definition:

$$V = \frac{3}{\beta_{ext}}$$

Note that this expression is for daytime, and that a different expression is used for the ASOS nighttime conversion. The total extinction provided by the Belfort sensor includes both Rayleigh and aerosol scattering, but aerosol scattering is generally the dominant effect, as pure Rayleigh scattering on an aerosol free day would yield a 550 nm visibility of over 250 km at sea level ($\beta_{Rayleigh} = 0.011\ km^{-1}$)[31], and typical measured visibility values are an order of magnitude

lower than that. Although no quality controls have been applied to the minute-by-minute unprocessed ASOS data, the individual data values can be filtered to yield reliable results according to recently presented criteria[32], namely:

1. the reported extinction value β_{ext} must fall into a range of 0.05 – 7.5 km^{-1}, corresponding to visibilities ranging from 0.25 – 60 miles,
2. the relative humidity must be less than or equal to 0.95,
3. the difference between an individual measurement and a three minute running average must be less than 20%, and
4. for multi-sensor sites, a three minute average of any two of the sensors should be less than 20%.

These criteria were designed for comparing ground-based data to satellite-derived values, which have a much larger field of view[32]. Thus, the fourth criterion, which is the most stringent in practice, rejects data that is likely accurate, but reflects disparate conditions between locations of the individual visibility sensors. The sensors are typically located 1 – 3 miles apart and are specifically sited to measure where "small [distance] scale variations are a) common and b) significant to airport operations,"[29]. However, the criteria do provide a useful metric for identifying data that is reliable. Additionally, this visibility data can be related to the aerosol optical depth (τ, AOD) which is measured during clear conditions by existing NASA assets; namely the AErosol RObotic NETwork (AERONET) system of aerosol monitoring stations[33], and the Moderate Resolution Imaging Spectroradiometer (MODIS) ground-observing satellites[34]. The AOD measured by AERONET and MODIS is a measure of the vertical optical attenuation on a path through the atmosphere, whereas the visibility and corresponding extinction coefficients provided by the ASOS stations are for a horizontal path. This difference is an important one because the aerosols are not evenly distributed as a function of altitude, and are instead strongly concentrated within a boundary layer near the Earth's surface, ranging up to a few kilometers in height. Furthermore, this distribution is not uniform, but rather varies strongly as a function of height[35,36]. However, comparisons between the horizontal visibility and vertical aerosol optical depth can be made by using scaling model relationships developed through semi-empirical fits of comparisons with measured data published in the literature, detailed in Table 1.

The units of the visibility in the equations shown are kilometers (km^{-1}), and the term z_a in Expressions 2 and 4 represents the aerosol scale height. The best values for the aerosol scale height z_a ranged between 1 and 2 for Ref. 32 and to 1.59-2.24 for three urban sites in Ref. 39. The AOD to Visibility conversion shown in Exp. 4 corresponds to values ~50% lower for clear conditions than the other expressions because the data for Seoul, Korea was heavily weighted to low visibility conditions[39], and will thus not be used for further analysis. It is clear that the expressions provided in Table 1 are not equivalent. This is due to the approximations made in going from measurements of a vertical column to a horizontal value, as well as the different locations considered in identifying these correlations (eastern United States, southern Germany, Cyprus and Korea, respectively).

Table 1: Equations for relating AOD τ to the horizontal visible extinction coefficient at ground.

Expression	AOD to Visibility	Correlation (R)	AOD Source	Reference
1	$V = \frac{3}{0.46\,\tau + 0.01}$	0.57	MODIS	[32]
2	$V = \frac{3.912 z_a}{\tau}$	0.90	AERONET	[37]
3	$V = \frac{3.9449}{\tau - 0.08498}$	0.76	MODIS	[38]
4	$V = 19.233 \cdot \exp\left(\frac{-\tau}{0.377 z_a}\right) + 2.910$	0.88	MODIS	[39]

The predictive capabilities using these expressions are fair, with correlational coefficients of 0.57-0.90. The correlations can be improved using refined modeling of the atmospheric aerosol profiles[32] or by improving the analysis algorithms of the AOD data[40]. It should also be noted that the AOD in Expression 1 is taken at a slightly different wavelength for the AERONET measurements than the MODIS measurements (500 nm vs. 550 nm, respectively). Both MODIS and AERONET only provide the AOD values for clear conditions, but the aerosol properties such as the Ångstrom coefficient and the size distribution do not generally change dramatically in short time periods and can be assumed to be similar to adjacent values, in contrast with the aerosol populations.

The extinction derived from the visibility is composed of two components: the aerosol extinction and the Rayleigh scattering ($\beta_{Rayleigh}$). The extinction due to Rayleigh scattering has a λ^{-4} spectral dependence (of blue sky fame), and is primarily important for short wavelengths. The wavelength dependence of the aerosol extinction $\beta_{ext,\,aerosol}$ follows a power law dependence, where the exponent is known as the Ångstrom coefficient (α). Large water droplets in clouds have a nearly flat spectral response, corresponding to an Ångstrom coefficient near zero, while the effective exponent for molecules undergoing Rayleigh scattering is four. Small particles have a spectral response between these extremes, with smaller particles being characterized with a larger Ångstrom coefficient and correspondingly larger changes in extinction with wavelength.

$$\beta_{\,aerosol}(\lambda_1) = \beta_{\,aerosol}(\lambda_0)\left(\frac{\lambda_1}{\lambda_0}\right)^{-\alpha}$$

The Ångstrom coefficient is a calculated product of the AERONET data, and multiple coefficients are provided in different wavelength ranges to scale the extinction appropriately, depending on the wavelength bands present at the AERONET site of interest. If available, the Level 1.5 cloud-screened data, or even better, the Level 2.0 quality assured AERONET data, should be used. Additionally, the Ångstrom coefficient derived using the spectral deconvolution algorithm (SDA) processing method covering the entire wavelength range should be

preferentially used if available. AERONET also provides aerosol size distributions which can also be useful for optical transport modeling. The procedure for scaling the total extinction to different wavelength values is to subtract out the Rayleigh scattering (0.011 km^{-1}) from the extinction value at 550 nm determined from the ASOS visibility, where the difference yields the aerosol extinction. The aerosol extinction can then be scaled using the Ångstrom coefficient, and the total extinction is then the sum of the updated aerosol extinction and the wavelength-appropriate Rayleigh scattering at that wavelength, which is tabulated in Ref. 31. This treatment neglects particle absorption, but that is generally a small effect for the near-ultraviolet to near-infrared wavelength range of interest here.

For measurements of the clouds themselves, LIDAR measurements provide the most useful data. Two ground-based LIDAR networks are currently operational, Micro-Pulse Lidar NETwork (MPLNET) in the United States and European Aerosol Research Lidar NETwork (EARLINET) in Europe, but the sites are relatively few in number and their data is only locally applicable. The Cloud-Aerosol Lidar with Orthogonal Polarization (CALIOP) instrument on the NASA-operated CALIPSO satellite is a space-based LIDAR instrument that can provide a great deal of information about atmospheric conditions, but the orbit does not cover all parts of the globe within a given day. In addition to the cloud structure, these LIDAR instruments can provide the extinction coefficient as a function of altitude and time of day above the sensor, but again the data is only useful for areas covered by their optical scans.

The methods described here provide a clear path towards calculating the visibility for various wavelength bands using measured data for a given location, time and date. Briefly, the process is as follows:

1. Look up sensor call signs for ASOS sites near the desired location.
2. Access data for the time and date of interest for each ASOS site in the 6405 one-minute data set. The first sensor should be regarded as the primary one, but the others can give insight on the data reliability if present.
3. The data should be compared to predicted ground extinction coefficients from AERONET and MODIS data if available. LIDAR data should also be used when available.
4. The AERONET Ångstrom coefficient should be used to relate the visible extinction coefficient at 550 nm to other wavelengths of interest. Specifically, the Rayleigh scattering ($\beta_{Rayleigh}$) is first subtracted from the total extinction (β_{ext}), to yield the aerosol extinction ($\beta_{aerosol}$). The aerosol extinction is scaled with the SDA Ångstrom coefficient, and then the wavelength-appropriate Rayleigh scattering added back in to acquire the total extinction at the new wavelength.
5. Cloud properties can be evaluated from MODIS and AERONET output, as well as LIDAR if available.

DISTRIBUTION

1	MS0406	Junoh Choi	5783
1	MS0892	Stephen Howell	1768
1	MS0968	Karen Rogers	5754
1	MS0968	Jeffrey Martin	5754
1	MS0968	Richard Harrison	5754
1	MS0968	Dora Wiemann	5754
1	MS0899	Technical Library	9536 (electronic copy)


Sandia National Laboratories